Alma Mater Studiorum · University of Bologna

School of Science
Department of Physics and Astronomy
Master Degree in Physics

Probing Anomalous Gluon Self-interaction at the LHC

Supervisor:
Prof. Fabio Maltoni

Co-supervisor:
Prof. Céline Degrande

Submitted by:
Matteo Maltoni

Academic Year 2019/2020

Contents

Abstract

The LHC experiment at CERN has established a golden era for precision measurements in particle physics, opening the possibility to detect deviations from the Standard Model predictions and constrain the new physics, up to the multi-TeV scales. In this work, a procedure is described to use this data to obtain bounds on a higher-dimensional operator, that describes new gluon self-interactions than the Standard Model ones, in an Effective Field Theory framework. In Chapter one, the Standard Model is breefly rehearsed: in Chapter two, the LHC main features are overviewed. In Chapter three, the Effective Field Theory approach is explained, with particular attention to the operator we are interested in this work; the previous works about it are summarised. Finally, in Chapter four, the possibility to constrain it by considering its interference with the Standard Model is detailedly explained, and some results from simulations are analysed.

1. The Standard Model: an introduction

The Standard Model (SM) is the name, given in the 1970s, to the theory describing the fundamental particles we know and how they interact. It explains three out of the four known fundamental forces in the universe, precisely predicting a wide variety of phenomena; over the years, it has become a well-tested physics theory.
In Fig. 1.0.1, the known SM particles are listed, with some parameters. All the known matter around us is made of particles, called *fermions* and occurring in two basic groups, the *quarks* and *leptons*. Each of these types consists of six particles (and the related antiparticles), coupled in three *generations* with similar features, but different masses. The stable matter in the universe is made of particles from the first, lightest generations: the *electron* and its *neutrino* for the leptons, and the *up* and *down quarks* for the quark sector. The other two generations are not stable, because of their higher masses: the *muon* and *tau* and their neutrinos for leptons, and the *charme* and *strange*, *top* and *bottom quarks*.
The electron, muon and tau all have an *electric charge* and a mass, while neutrinos are electrically chargeless and massless. Quarks, in addition to these properties, present a *color charge* and only mix in order to form colorless objects.
The electromagnetic, weak and strong interactions between these states are described, in the SM framework, through the exchange of other particles, called *bosons*, which carry discrete amounts of energy from one fermion to another. The strong force is carried by *gluons*, the weak one by W and Z *bosons*, the electromagnetic one by *photons*. The last interaction has an infinite range, while the other two have a finite one; photons and gluons are massless, while the weak bosons show a mass because of their interaction with the *Higgs boson*, the last-discovered particle in the SM, and the only scalar boson in it.
Gravity, the only other known force, is still not incorporated in the model, since a quantum version of General Relativity has not been proved to be reliable so far. Despite this, SM predictions are correct enough in many cases, because the effect of gravity is negligible at particle scales.

1.1. The gauge principle

In the last century, symmetries have played a major role in the development of physical theories[1]. As the *Noether theorem* states, if an action is invariant under a certain transformation group, one or more conserved quantities exist, which are associated to the it. Starting from this, Salam and Ward[2] introduced the gauge principle as a basis for constructing quantum field theories of interacting fields: by making local gauge transformations on the free Lagrangian and requiring its conservation, interaction terms appear, with all their symmetry properties.
Let us start from the free Dirac Lagrangian, for a fermion ψ,

$$\mathcal{L}_0 = \bar{\psi}\left(i\not{\partial} - m\right)\psi \tag{1.1.1}$$

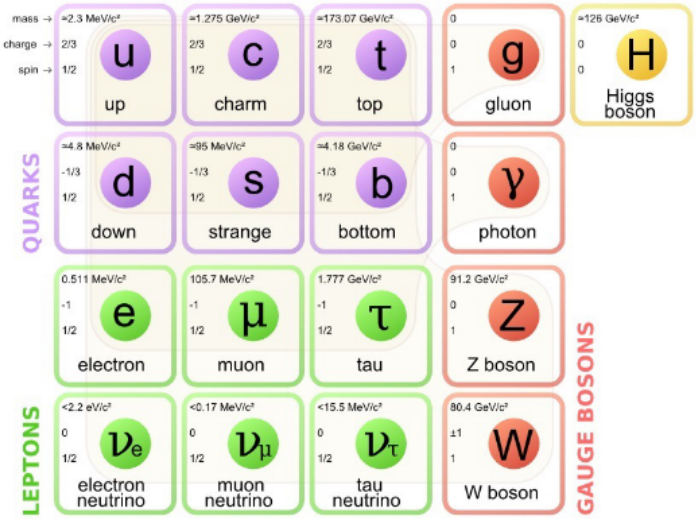

FIGURE 1.0.1. The fundamental particles predicted by the Standard Model, with their mass, electric charge and spin

and apply a local U(1) transformation $\psi \rightarrow \psi^{'}(x) = e^{-i\alpha(x)}\psi(x)$, with the parameter α varying over spacetime; the Lagrangian does not remain invariant, since

$$\mathcal{L}_0 \rightarrow \mathcal{L}^{'} = \mathcal{L}_0 + \bar{\psi}\gamma^{\mu}\psi\,\partial_{\mu}\alpha. \tag{1.1.2}$$

$\mathcal{L}_0$, though, is invariant under global U(1) transformations; in order to maintain the same property for local changes, we modify the derivative through the *minimal coupling*, by introducing a *gauge field* A_{μ}, as

$$\mathcal{D}_{\mu} = \partial_{\mu} + ieA_{\mu}. \tag{1.1.3}$$

In this way, we obtain the Lagrangian conservation by asking the gauge field to transform as

$$A_{\mu} \rightarrow A_{\mu}^{'} = A_{\mu} + \frac{1}{e}\partial_{\mu}\alpha. \tag{1.1.4}$$

The gauge field A_{μ} is interpretable as the electromagnetic (EM) one, so that photons existence follows from th invariance under U(1) transformations; the coupling e between this field and the fermionic one plays the role of the electric charge, and is conserved because of Noether theorem. Since the EM strength tensor $F_{\mu\nu} = \partial_{\mu}A_{\nu} - \partial_{\nu}A_{\mu}$ is invariant under (1.1.4), we obtain the Quantum Electrodynamics (QED) Lagrangian by adding the free gauge field term to the Dirac Lagrangian,

$$\mathcal{L}_{QED} = \bar{\psi}\left(i\not{\mathcal{D}} - m\right)\psi - \frac{1}{4}F_{\mu\nu}F^{\mu\nu}. \tag{1.1.5}$$

It is important to stress that a mass term for the gauge field

$$\mathcal{L}_A^m = -\frac{1}{2}A_{\mu}A^{\mu}, \tag{1.1.6}$$

is not invariant under (1.1.4), so that something has to be added for a massive vector boson gauge-invariant theory.

The same idea can be generalised to non-abelian interactions, realted to symmetries whose generators do not commute, contrarily to the U(1) case, but satisfy a relation

$$[t_a, t_b] = iC_{abc}t_c, \tag{1.1.7}$$

with C_{abc} the structure constants of the group. We want the Lagrangian to be invariant under local field transformations of the kind $\psi \to \psi'(x) = \Omega(x)\psi(x) = e^{-iT^a\alpha^a(x)}\psi(x)$, with T^a a representation of the generators t^a. As in the abelian case, we define the covariant derivative as

$$\mathcal{D}_\mu = \partial_\mu - igT^aA^a_\mu, \tag{1.1.8}$$

with A^a_μ the gauge field; a is the gauge index. By requiring the Lagrangian conservation, we obtain the transformation law

$$A^a_\mu \ \to \ A^{a'}_\mu = A^a_\mu - \frac{1}{g}\partial_\mu\alpha^a + C_{abc}\alpha^bA^c_\mu, \tag{1.1.9}$$

which contains an additional term than the abelian case (1.1.4), due to the non-commutativity of the generators. If generalising the strength tensor to

$$F^a_{\mu\nu} = \partial_\mu A^a_\nu - \partial_\nu A^a_\mu + gC_{abc}A^b_\mu A^c_\nu, \tag{1.1.10}$$

the gauge boson kinetic term can be written, analogously to the abelian case, as

$$\mathcal{L}_A = -\frac{1}{4}F^a_{\mu\nu}F^{a,\mu\nu}. \tag{1.1.11}$$

This term, when explicitly written, presents self-interactions, for the gauge bosons, which are not present for the abelian ones, under the appearance of three- and four-vertices.
The non-abelian case includes the strong and weak interactions: in the first case, the symmetry group is U(3), with 8 generators, so that there are 8 gauge bosons, called gluons, and the conserved charge is the color one; in the second case, the group is U(2) and 3 generators are present, with the weak isospin I as conserved charge.
A mass term for the gauge bosons is still not gauge-invariant: Spontaneuos Symmetry Breaking and the Higgs mechanism are needed to handle massive gauge bosons, like the weak ones.

1.2. Constructing the electroweak model

Since the 1950s, several attempts were made to build a gauge theory for the electroweak (EW) interaction. Glashow[3] suggested a gauge group SU(2) $\otimes$ U(1), with the latter associated to the *leptonic hypercharge* Y, satisfying the Gell-Mann-Nishijina relation $Q = I_3 + Y/2$. Four gauge bosons are needed, but their mass terms explicitly break gauge invariance, as we saw before. Weinberg[4] and Salam introduced the Higgs mechanism to give mass to these bosons, while preserving gauge invariance and, thus, renormalisability: the Glashow-Weinberg-Salam model is know as the *Standard Model of EW interactions*.
Experiments have shown that the weak current only involves left-handed fermions, so that it can be written as

$$\bar{\psi}_L\gamma^\mu\psi_L = \frac{1}{2}\bar{\psi}\gamma^\mu(1-\gamma_5)\psi. \tag{1.2.1}$$

In the following, we will use $\ell = \{e, \mu, \tau\}$ for lepton flavours and ν for neutrinos. We introduce the left-handed isospin doublet

$$L = \begin{pmatrix} \nu \\ \ell \end{pmatrix}_L = \begin{pmatrix} \nu_L \\ \ell_L \end{pmatrix}, \tag{1.2.2}$$

with isospin $I = 1/2$ and $I_3 = \pm 1/2$ for the neutrino and the lepton, respectively. Since neutrinos are considered as massless in the model, no right-handed term is present for them, and the right-handed lepton is considered as a weak isospin singlet $R = \ell_R$, with $I = 0$.
Using this notation and Pauli matrices τ^i, the weak current (1.2.1) can be written as

$$J^i_\mu = \bar{L}\gamma_\mu \frac{\tau^i}{2} L. \tag{1.2.3}$$

By writing them explicitly, it is easy to see that J^1_μ and J^2_μ mix up and down components of the isospin doublet: the charged current, that couples with the intermediate vector boson $W^\pm_\mu$, can be written as a combination of those two, as

$$J^\mp_\mu = 2(J^1_\mu \pm i J^2_\mu). \tag{1.2.4}$$

Then, we can define the hypercharge current

$$J^Y_\mu = -(\bar{L}\gamma_\mu L + 2\bar{R}\gamma_\mu R) \tag{1.2.5}$$

and combine it with the neutral current J_3, in order to obtain a current, whose time-like component is associated to the electric charge:

$$J^{em}_\mu = J^3_\mu + \frac{1}{2} J^Y_\mu = -\bar{\ell}\gamma_\mu \ell. \tag{1.2.6}$$

This is the electromagnetic current and the Gell-Mann-Nishijina relation naturally emerges from it.
We now have to introduce a gauge field for each generator: W^1_μ, W^2_μ, W^3_μ for $\mathrm{SU}(2)_L$ and B_μ for $\mathrm{U}(1)_Y$, with field strengths

$$\begin{aligned} W^i_{\mu\nu} &= \partial_\mu W^i_\nu - \partial_\nu W^i_\mu + g\varepsilon^{ijk} W^j_\mu W^k_\nu, \\ B_{\mu\nu} &= \partial_\mu B_\nu - \partial_\nu B_\mu. \end{aligned} \tag{1.2.7}$$

The fermion-gauge boson couplings are given by the covariant derivatives, which are different for the left- and right-handed components, since the right ones do not feel the charged weak interaction:

$$\begin{aligned} \mathcal{L} = &-\frac{1}{4} W^i_{\mu\nu} W^{i,\mu\nu} - \frac{1}{4} B_{\mu\nu} B^{\mu\nu} \\ &+ \bar{L} i\gamma^\mu \left(\partial_\mu + i\frac{g}{2}\tau^i W^i_\mu + i\frac{g'}{2} Y B_\mu\right) L + \bar{R} i\gamma^\mu \left(\partial_\mu + i\frac{g'}{2} Y B_\mu\right) R. \end{aligned} \tag{1.2.8}$$

The Lagrangian above contains the term

$$\begin{aligned} \mathcal{L}_{lept} \supset &-\frac{g}{2}\bar{L}\gamma^\mu \begin{pmatrix} 0 & W^1_\mu - iW^2_\mu \\ W^1_\mu + iW^2_\mu & 0 \end{pmatrix} L \\ &- \frac{g}{2}\bar{L}\gamma^\mu \tau^3 L W^3_\mu - \frac{g'}{2}(\bar{L}\gamma^\mu Y L + \bar{R}\gamma^\mu Y R) B_\mu, \end{aligned} \tag{1.2.9}$$

so that it is straightforward to define the charged gauge bosons as

$$W_\mu^\pm = \frac{1}{\sqrt{2}}(W_\mu^1 \mp W_\mu^2) \tag{1.2.10}$$

and to rotate the neutral fields, in order to obtain the EM and the neutral weak fields

$$\begin{pmatrix} A_\mu \\ Z_\mu \end{pmatrix} = \begin{pmatrix} \cos\theta_W & \sin\theta_W \\ -\sin\theta_W & \cos\theta_W \end{pmatrix} \begin{pmatrix} B_\mu \\ W_\mu^3 \end{pmatrix}. \tag{1.2.11}$$

A_μ is the field combination that actually couples with the EM current; θ_W is called *Weinberg angle* and fulfils the relation

$$\cos\theta_W = \frac{g}{\sqrt{g^2+g'^2}}. \tag{1.2.12}$$

In terms of the new fields, the leptonic Lagrangian becomes

$$\mathcal{L}_{lept} = -\frac{g}{2\sqrt{2}}[\bar{\nu}\gamma^\mu(1-\gamma_5)\ell\, W_\mu^+ + \bar{\ell}\gamma^\mu(1-\gamma_5)\nu\, W_\mu^-] \tag{1.2.13}$$

$$- g\sin\theta_W\, \bar{\ell}\gamma^\mu\ell\, A_\mu - \frac{g}{2\cos\theta_W}\sum_{\psi_i=\nu,\ell} \bar{\psi}_i\gamma^\mu(g_V^i - g_A^i\gamma_5)\psi_i\, Z_\mu. \tag{1.2.14}$$

The Z boson mediates weak interactions without change of charge, and it couples with fermions in a vectorial and an axial ways. By looking at the EM term, one can easily identify the electric charge as

$$e = g\sin\theta_W = g'\cos\theta_W. \tag{1.2.15}$$

So far, the theory describes massless fermions ν, ℓ and four massless gauge fields $W_\mu^\pm$, Z_μ and A_μ; Spontaneous Symmetry Breaking (SSB) and the Higgs mechanism have to be added to give mass to the ℓ fermions and to three of the gauge bosons, leaving the photon as massless.

1.3. The Higgs mechanism

Let us introduce a scalar doublet

$$\Phi = \begin{pmatrix} \phi^+ \\ \phi^0 \end{pmatrix} \tag{1.3.1}$$

with hypercharge $Y = 1$. Its Lagrangian reads

$$\mathcal{L}_{scal} = \mathcal{D}_\mu\Phi^\dagger\mathcal{D}^\mu\Phi - \mu^2\Phi^\dagger\Phi - \lambda(\Phi^\dagger\Phi)^2, \tag{1.3.2}$$

with the covariant derivative given by

$$\mathcal{D}_\mu = \partial_\mu + ig\frac{\tau^i}{2}W_\mu^i + i\frac{g'}{2}YB_\mu. \tag{1.3.3}$$

With this choice of the potential, the symmetry is spontaneously broken, since the Lagrangian is invariant under field rotations, but the vacuum is not. We choose the Higgs field vacuum expectation value (vev) as

$$\langle\Phi\rangle_0 = \begin{pmatrix} 0 \\ \sqrt{-\mu^2/2\lambda} \end{pmatrix} = \begin{pmatrix} 0 \\ v/\sqrt{2} \end{pmatrix}. \tag{1.3.4}$$

This vacuum expression is invariant under $\mathrm{U}(1)_{em}$, since

$$e^{i\alpha Q}\langle\Phi\rangle_0 \approx (1+i\alpha Q)\langle\Phi\rangle_0 = \langle\Phi\rangle_0 + i\alpha\left(I_3+\frac{Y}{2}\right)\langle\Phi\rangle_0$$
$$= \langle\Phi\rangle_0 + \frac{1}{2}\left[\begin{pmatrix}1&0\\0&-1\end{pmatrix}+\begin{pmatrix}1&0\\0&1\end{pmatrix}\right]\begin{pmatrix}0\\v/\sqrt{2}\end{pmatrix} = \langle\Phi\rangle_0. \quad (1.3.5)$$

This is not valid for the other generators T_1, T_2 and $T_3 - Y/2$, which are called *broken* for this reason; this means that the originally symmetry group $\mathrm{SU}(2)_L \otimes \mathrm{U}(1)_Y$, of dimension 4, is spontaneously broken into $\mathrm{U}(1)_{em}$, of dimension 1, which remains as a symmetry of the vacuum. At the end of the process, the three weak bosons will acquire mass, while the photon will not.
In order to make this explicit, we write the Higgs doublet in the unitary gauge, as small oscillations around the vacuum,

$$\Phi = \frac{v+H}{\sqrt{2}}\begin{pmatrix}0\\1\end{pmatrix}, \quad (1.3.6)$$

so that the scalar Lagrangian can be written as

$$\mathcal{L}_{scal} = \left|\left(\partial_\mu + ig\frac{\tau^i}{2}W^i_\mu + i\frac{g'}{2}YB_\mu\right)\frac{v+H}{\sqrt{2}}\begin{pmatrix}0\\1\end{pmatrix}\right|^2 \quad (1.3.7)$$
$$-\frac{\mu^2}{2}(v+H)^2 - \frac{\lambda}{4}(v+H)^4.$$

The term in the first line contains the vector bosons: in terms of the physical fields, it reads

$$\frac{1}{2}\partial_\mu H\partial^\mu H + \frac{g^2}{4}(v+H)^2\left(W^+_\mu W^{-\mu} + \frac{1}{2\cos^2\theta_W}Z_\mu Z^\mu\right)$$
$$= \frac{1}{2}\partial_\mu H\partial^\mu H + \frac{g^2v^2}{4}W^+_\mu W^{-\mu} + \frac{g^2v^2}{8\cos^2\theta_W}Z_\mu Z^\mu + \dots, \quad (1.3.8)$$

from which we can identify

$$M_W = \frac{gv}{2}, \qquad M_Z = \frac{gv}{2\cos\theta_W} = \frac{M_W}{\cos\theta_W}. \quad (1.3.9)$$

On the other hand, no quadratic term in A_μ appears, so the photon remains massless, as it was expected from the $\mathrm{U}(1)_{em}$ symmetry.
The second line in (1.3.7) contains terms only involving the Higgs scalar field: its mass can be written as

$$M_H = \sqrt{-2\mu^2}. \quad (1.3.10)$$

The value of v can be determined from the Fermi constant one, by matching the SM predictions with the low energy phenomenology, leading to $v \approx 246$ GeV. By assuming an experimental magnitude for $\sin^2\theta_W \approx 0.22$, we obtain for the weak bosons masses $M_W \approx 80$ GeV, $M_Z \approx 90$ GeV. The Higgs mass value, though, cannot be determined, since μ^2 remains a free parameter of the theory.

The lepton masses come from their Yukawa couplings to the Higgs, which are described by the Lagrangian term

$$\begin{aligned}\mathcal{L}_{Yuk} &= -y_\ell(\bar{R}\Phi^\dagger L + \bar{L}\Phi R) \\ &= -y_\ell\frac{v+H}{\sqrt{2}}\left[\bar{\ell}_R(0\ \ 1)\begin{pmatrix}\nu_L\\ \ell_L\end{pmatrix} + (\bar{\nu}_L\ \ \bar{\ell}_L)\begin{pmatrix}0\\1\end{pmatrix}\ell_R\right] \\ &= -\frac{y_\ell v}{\sqrt{2}}\bar{\ell}\ell - \frac{y_\ell}{\sqrt{2}}\bar{\ell}\ell H.\end{aligned} \tag{1.3.11}$$

It can be seen that the neutrinos remain massless, while ℓ leptons gain a mass term

$$M_\ell = \frac{y_\ell v}{\sqrt{2}}. \tag{1.3.12}$$

This is generated in a gauge-invariant way, but the mass values are not specified, since the Yukawa couplings are free parameters. The couplings between the Higgs and the fermions depend on the latter masses, as

$$C_{\bar{\ell}\ell H} = \frac{y_\ell}{\sqrt{2}} = \frac{M_\ell}{v}. \tag{1.3.13}$$

1.4. The strong-interacting particles

The observation of exotic particles suggested the existence of fundamental states, with an additional charge called *color*. These particles are called *quarks* and they can experience the strong interaction, due to their charge. In analogy to what had been done for leptons, Glashow, Iliopoulos and Maiani proposed the GIM mechanism[5]: they introduced the weak doublets

$$\begin{aligned}L_U &= \begin{pmatrix}u\\ d'\end{pmatrix}_L = \begin{pmatrix}u\\ d\cos\theta_C + s\sin\theta_C\end{pmatrix}_L, \\ L_C &= \begin{pmatrix}c\\ s'\end{pmatrix}_L = \begin{pmatrix}c\\ -d\sin\theta_C + s\cos\theta_C\end{pmatrix}_L\end{aligned} \tag{1.4.1}$$

and the right-handed singlets $R_U = u_R$, $R_D = d_R$, $R_S = s_R$, $R_C = c_R$. d', s' are interaction eigenstates, related to the mass ones through the Cabibbo angle θ_C, introduced to make the hadronic current universal, with a common coupling constant. As in the leptonic case, by starting from the free massless Dirac Lagrangian for the quarks, one can add the gauge boson interactions through the covariant derivatives, with the hypercharges determined by the Gell-Mann-Nishijina relation, in order to have the up-like quark electric charges equal to +2/3, and the down-like ones to -1/3, as observations request:

$$Y_L = \frac{1}{3}, \quad Y_{R_U} = \frac{4}{3}, \quad Y_{R_D} = -\frac{2}{3}. \tag{1.4.2}$$

The charged and neutral weak currents can be written as

$$\begin{aligned}\mathcal{L}_q = &\frac{g}{2\sqrt{2}}[\bar{u}\gamma^\mu(1-\gamma_5)d' + \bar{c}\gamma^\mu(1-\gamma_5)s']W^+_\mu + \text{h.c.} \\ &- \frac{g}{2\cos\theta_W}\sum_{\psi_q=u,\dots,c}\bar{\psi}_q\gamma^\mu(g^q_V - g^q_A\gamma_5)\psi_q\, Z_\mu,\end{aligned} \tag{1.4.3}$$

where the vectorial and axial couplings appear.
Some loop corrections in field theory can violate a classical conservation law, breaking gauge invariance and the renormalisability of the theory. These are called *anomalies* and their cancellation is required for theories to be realistic. The SM is free from anomalies if fermions appear in complete multiplets, repeating the same structure

$$\left\{\begin{pmatrix}\nu_e\\ e\end{pmatrix}_L,\ e_R,\ \begin{pmatrix}u\\ d\end{pmatrix}_L,\ u_R,\ d_R\right\},$$
$$\left\{\begin{pmatrix}\nu_\mu\\ \mu\end{pmatrix}_L,\ \mu_R,\ \begin{pmatrix}c\\ s\end{pmatrix}_L,\ c_R,\ s_R\right\},$$
$$\left\{\begin{pmatrix}\nu_\tau\\ \tau\end{pmatrix}_L,\ \tau_R,\ \begin{pmatrix}t\\ b\end{pmatrix}_L,\ t_R,\ b_R\right\}.$$

These are called *generations*; the last one was discovered later than the others, under the guidance of the anomalies cancellation principle.
The Higgs mechanism provides mass terms for the up- and down-type quarks, too. If we define the conjugate Higgs doublet as

$$\tilde{\Phi} = i\sigma_2\Phi^* = \begin{pmatrix}\phi^{0*}\\ -\phi^-\end{pmatrix}, \tag{1.4.4}$$

the Yukawa Lagrangian for the quark generations reads

$$\mathcal{L}_{Yuk} = -\sum_{i,j=1}^{3}\left(Y^U_{ij}\bar{R}_{U_i}\tilde{\Phi}^\dagger L_j + Y^D_{ij}\bar{R}_{D_i}\Phi^\dagger L_j\right) + \text{h.c.}. \tag{1.4.5}$$

By substituting the vacuum expectation values of the doublets, one obtains the mass matrices

$$\mathcal{M}^{U(D)}_{ij} = \frac{v}{\sqrt{2}}Y^{U(D)}_{ij}, \tag{1.4.6}$$

which are not diagonal, since they are written in the interaction basis. Two unitary transformations of the fields have to be performed, to turn them into mass eigenstates:

$$\begin{pmatrix}u'\\ c'\\ t'\end{pmatrix}_{L,R} = U_{L,R}\begin{pmatrix}u\\ c\\ t\end{pmatrix}_{L,R}, \qquad \begin{pmatrix}d'\\ s'\\ b'\end{pmatrix}_{L,R} = D_{L,R}\begin{pmatrix}d\\ s\\ b\end{pmatrix}_{L,R}. \tag{1.4.7}$$

The unitarity of $U_{L,R}$ and $D_{L,R}$ is necessary to maintain the kinetic terms form. The mass matrices get diagonalised as

$$U_R^{-1}\mathcal{M}^U U_L = \begin{pmatrix}m_u & 0 & 0\\ 0 & m_c & 0\\ 0 & 0 & m_t\end{pmatrix}, \quad D_R^{-1}\mathcal{M}^D D_L = \begin{pmatrix}m_d & 0 & 0\\ 0 & m_s & 0\\ 0 & 0 & m_b\end{pmatrix}. \tag{1.4.8}$$

The neutral weak current for quarks is proportional to

$$(\bar{u}',\ \bar{c}',\ \bar{t}')_L\gamma_\mu\begin{pmatrix}u'\\ c'\\ t'\end{pmatrix}_L = (\bar{u},\ \bar{c},\ \bar{t})_L\,(U_L^\dagger U_L)\,\gamma_\mu\begin{pmatrix}u\\ c\\ t\end{pmatrix}_L, \tag{1.4.9}$$

so that no mixing is present in this sector, since U_L is unitary. The charged weak current, on the other hand, is proportional to

$$(\bar{u}', \ \bar{c}', \ \bar{t}')_L \gamma_\mu \begin{pmatrix} d' \\ s' \\ b' \end{pmatrix}_L = (\bar{u}, \ \bar{c}, \ \bar{t})_L \, (U_L^\dagger D_L) \, \gamma_\mu \begin{pmatrix} d \\ s \\ b \end{pmatrix}_L . \tag{1.4.10}$$

The mixing matrix $V = U_L^\dagger D_L$ is called *Cabibbo-Kobayashi-Maskawa* (CKM) matrix; being a U(3) one, it depends on nine real parameters, of which three are rotation angles and six are phases. Five of the latters can be reabsorbed through left-handed quark phase transformations, so in the end the CKM matrix can be parametrised using three angles θ_{12}, θ_{13}, θ_{23} and a phase δ_{13}, as

$$V = R_1(\theta_{23}) \, R_2(\theta_{13}, \delta_{13}) \, R_3(\theta_{12}), \tag{1.4.11}$$

with $R_i(\theta_{jk})$ rotation matrices around the i^{th} axis, mixing the j^{th} and k^{th} generations. For three generations, it is not always possible to choose V to be real, say $\delta_{13} = 0$: weak interactions can violate CP and T symmetries. The entries of the V matrix, assuming three generations and, thus, unitarity constraints, are measured through weak quark decays and deep inelastic neutrino scattering; experimentally, one has $0 < \sin\theta_{13} \ll \sin\theta_{23} \ll \sin\theta_{12} \ll 1$.
The extension of the EW model to the strong interactions is straightforward: once SU(3) field strengths $G^A_{\mu\nu}$ and gluon fields have been introduced, the quarks covariant derivatives can be modified by adding a term proportional to the strong coupling g_S. The final symmetry group of the SM is, thus, $\mathrm{SU}(3)_C \otimes \mathrm{SU}(2)_L \otimes \mathrm{U}(1)_Y$. Before the SSB, related to the Higgs mechanism, the Lagrangian of the SM of strong and EW interactions reads

$$\begin{aligned} \mathcal{L}_{SM} = & -\frac{1}{4} G^A_{\mu\nu} G_A^{\mu\nu} - \frac{1}{4} W^I_{\mu\nu} W_I^{\mu\nu} - \frac{1}{4} B_{\mu\nu} B^{\mu\nu} + \mathcal{D}_\mu \Phi^\dagger \mathcal{D}^\mu \Phi - \mu^2 \Phi^\dagger \Phi - \lambda (\Phi^\dagger \Phi)^2 \\ & + \sum_{\ell = e,\mu,\tau} [\bar{L} i \not{\mathcal{D}} L + \bar{R} i \not{\mathcal{D}} R - y_\ell (\bar{L} \, \Phi R + \text{h.c.})] \\ & + \sum_{colors} \sum_{j=1}^{3} \left[\bar{u}_j i \not{\mathcal{D}} u_j + \bar{d}_j i \not{\mathcal{D}} d_j - \sum_{k=1}^{3} \left(\bar{q}_{jL} \, \Phi Y^D_{jk} d_{kR} + \bar{q}_{jL} \, \tilde{\Phi} Y^U_{jk} u_{kR} + \text{h.c.} \right) \right], \end{aligned} \tag{1.4.12}$$

where $q_{iL} = \begin{pmatrix} u_{iL} \\ d_{iL} \end{pmatrix}$. After the SSB, in the mass eigenstates basis, the Lagrangian becomes

$$\begin{aligned} \mathcal{L}_{SM} = & -\frac{1}{4} G^A_{\mu\nu} G_A^{\mu\nu} - \frac{1}{4} W^I_{\mu\nu} W_I^{\mu\nu} - \frac{1}{4} B_{\mu\nu} B^{\mu\nu} \\ & + \frac{1}{2} \partial_\mu H \partial^\mu H - \frac{M_H^2}{2} H^2 - \lambda v H^3 - \frac{\lambda}{4} H^4 + \left(M_W^2 W^{+\mu} W^-_\mu + \frac{M_Z^2}{2} Z^\mu Z_\mu \right) \left(1 + \frac{H}{v} \right)^2 \\ & + \sum_{\ell = e,\mu,\tau} [\bar{L} i \not{\mathcal{D}} L + \bar{R} i \not{\mathcal{D}} R - M_\ell \bar{\ell} \ell] \end{aligned} \tag{1.4.13}$$

$$+\sum_{colors}\sum_{j=1}^{3}\left[\bar{u'}_j i\not{D} u'_j+\bar{d'}_j i\not{D} d'_j-(M_j^U\bar{u'}_j u'_j+M_j^D\bar{d'}_j d'_j)\left(1+\frac{H}{v}\right)^2\right]$$
$$+A_\mu J^\mu_{em}+Z_\mu J^\mu_0+W^+_\mu J^\mu_+ + W^-_\mu J^\mu_-.$$

The currents in the last line contain the interaction terms:

$$J^\mu_{em}=-e\sum_{i=1}^{3}\left[\bar{\ell}_i\ell_i+\sum_{colors}\left(\frac{1}{3}\bar{d'}_i\gamma^\mu d'_i-\frac{2}{3}\bar{u'}_i\gamma^\mu u'_i\right)\right],$$
$$J^\mu_+=\frac{g}{\sqrt{2}}\sum_{i=1}^{3}\left(\bar{\nu}_i\gamma^\mu\ell_{iL}+\sum_{colors}\bar{u'}_{iL}\gamma^\mu\, V\, d'_{iR}\right)=(J^\mu_-)^\dagger,$$
$$J^\mu_0=\frac{1}{2\cos\theta_W}\sum_{i=1}^{3}\Big[\bar{\nu}_i\gamma^\mu\nu_i-\bar{\ell}_{iL}\gamma^\mu\ell_{iR}+2\bar{\ell}_i\gamma^\mu\ell_i\sin^2\theta_W$$
$$+\bar{u'}_{iL}\gamma^\mu u'_{iL}-\bar{d'}_{iL}\gamma^\mu d'_{iL}+\left(\frac{2}{3}\bar{d'}_i\gamma^\mu d'_i-\frac{4}{3}\bar{u'}_i\gamma^\mu u_i\right)\sin^2\theta_W\Big].$$

Now, we should quantise it and show it is renormalisable; in the end, one remains with a renormalised and anomaly-free theory, which describes the physics below the EW energy scale v.

2. Introduction to LHC physics

2.1. Overview of the accelerator

The Large Hadron Collider (LHC) is a proton-proton collider located at CERN, in Geneva[6]; it started working in 2008. It can reach a center-mass-energy $\sqrt{s} = 13$ TeV and an integrated luminosity

$$\int \mathcal{L}\, dt \approx 100\,\text{fb}^{-1} \text{ per year.}$$

The accelerator is built in the LEP tunnel, which has a circumference of 27 km: the ring contains superconducting magnets and accelerating structures, to boost the particles. The beams are distributed in 2750 bunches of $\sim 10^{11}$ protons each; two high-energy beams travel one against the other and collide. They are giuded by a strong magnetic field, maintained by electromagnets in the superconducting state; liquid helium is used to cool them down to the temperature requested for this condition. Most of the produced tracks are soft and can be separated from the interesting interactions. The high luminosity value assures heavy particles to be produced with high statistics, as it can be seen from Table 2.1. The SM processes that we already observed in the past decades are abundantly produced, yielding a large background for new physics discoveries and helping to reduce the systematic errors.
A scheme of the accelerator complex is shown in Fig. 2.1.1. The LHC is made of eight sectors, separated by insertions which can work for injection, beam dumping, beam cleaning, or beam collision. Along each sector, 154 dipoles are located to bend the particles trajectories. Different kinds of magnets are present: dipoles maintain beams along a circular orbit, while quadrupoles reduce the beams size to maximise the number of proton-proton collisions. The maximum reachable energy is directly dependent on the dipole field intensity, which can get to 8.3 T; to do so, they have to work at 1.9 K, even a lower temperature than the outer space one. Moreover, a series of machines accelerates the protons up to intermediate energies, before injecting them into the main ring: Linac 2, Proton Synchroton Booster (PSB), Proton Synchroton (PS), Super Proton Synchroton (SPS).
Protons are sourced from a tank of hydrogen gas, where an electric field divides the electrons from the nuclei. After the acceleration, beams travel for hours inside the beam pipes, and finally collide inside four detectors: ATLAS, CMS, ALICE, LHCb.

Process	σ	Events/s	Events/year
$W \to e\nu$	15 nb	15	10^8
$Z \to ee$	1.5 nb	1.5	10^7
$\bar{t}t$	800 pb	0.8	10^7
$\bar{b}b$	500 μb	10^5	10^{12}

TABLE 2.1. Typical values of expected events for processes of interest at the LHC, for an integrated luminosity of 10 fb^{-1} per year[6]

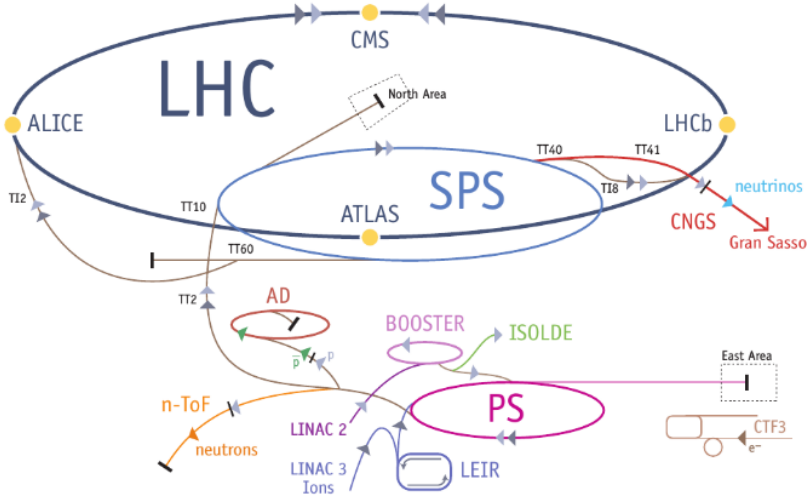

FIGURE 2.1.1. Scheme of the LHC accelerator complex at CERN

2.2. The LHC detectors

The main characteristics that are required for detectors are speed, to not integrate over too many bunch crossings; granularity, to avoid the same detector to be crossed by particles from more than one interaction; radiation hardness, since the particle fluxes deposit considerable amounts of energy.
Since we do not know which signatures the new physics would bring, they have to be sensitive to all the particles that can be produced in the interactions. The main detectors, ATLAS and CMS, are composed by many sub-ones, each of them with a specific task for reconstructing the events. Their basic structure is similar:

- the track momenta and charges, as the secondary vertexes, are measured in the central tracker;
- electromagnetic calorimeters are used to measure electrons and photons energy and position, excellent position and energy resolutions are required;
- hadronic calorimeters measure hadrons and jets energy and position, granularity is required;
- muons are identified in an external spectrometer, that also measures their momenta;
- neutrinos are detected through missing transverse energy measurements, through calorimeters over a pseudorapidity range $|\eta| < 5$.

In Fig. 2.2.1, the ATLAS and CMS detectors are shown, with some of their components.
For ATLAS, the tracking section is built of silicon pixel and is immersed in a solenoidal field of 2 T. Behind the solenoid, a liquid argon calorimeter, showing a high granularity, and an iron-scintillator hadronic calorimeter are present. Around them, muon gas detectors are arranged in a toroidal magnetic field.
For the CMS, the tracking is made of silicon detectors; the electromagnetic calorimeter

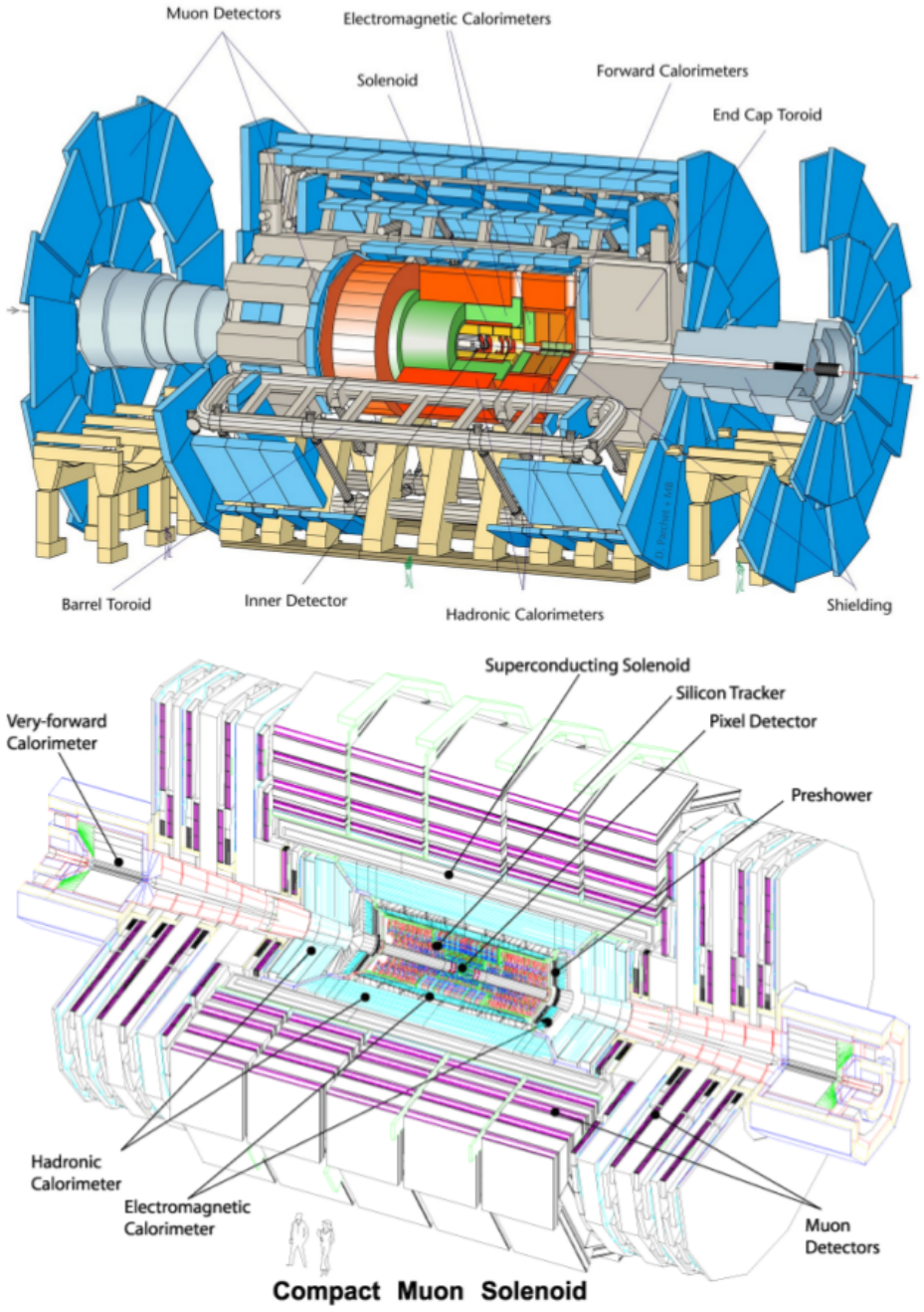

FIGURE 2.2.1. Exploded views of the ATLAS and CMS detectors[6]

contains $PbWO_4$ crystals, while the hadronic calorimeter is built of copper, with scintillator readout. These components lie inside a solenoidal field of 4 T; all outside, muon chambers are inserted in iron.
The two main detectors have similar performance goals in detecting physical objects:

- lepton measurement: lepton transverse momenta can be measured in a range between 1 GeV and 5 TeV;

- mass resolution: for a mass $\sim$ 100 GeV, resolutions of 1% for leptonic peaks and 10% for jet-jet peaks are assured;
- the calorimeters cover a pseudorapidity range $|\eta| < 5$;
- particle identification: some typical detection efficiencies are $\epsilon_b \sim 60\%$, $\epsilon_\tau \sim 50\%$, $\epsilon_\gamma \sim 80\%$, $\epsilon_e \sim 50\%$;
- Trigger: the beam crossing rate is of 40 MHz, but the output to the event storage is limited to 100 Hz. The detectors are, thus, equipped with a multi-state selection system, which must provide a high efficiency for the interesting events.

The high-energy events are dominated by QCD jets production and experimental techniques have been developed to reject them.

2.2.1. Electron-photon identification

Electrons and photons need to be isolated from the QCD jets background. The ATLAS Collaboration handles the problem by studying the longitudinal and lateral energy deposition pattern of the jets; the calorimeters have to be suitably placed laterally and longitudinally, to achieve a sufficient rejection. After this, the sample is mainly constitued of EM objects, which means electrons, photons and a jet background, due to quarks and gluons combining in π^0 and then decaying in two photons. These decay products can be isolated from the others by looking for their two-body spectra in the calorimeter depositions: a high granularity of these detectors is requested.
A track from $\pi^\pm$ over an EM cluster can mock an electron signature: these cases can be rejected by requiring a match between the position and momentum of the track and of the cluster. A high resolution in EM energy and position measurements is needed.

2.2.2. τ hadronic decays

The τ mainly decays into one or three charged particles, plus some π^0 particles. Because of τ large mass, the high momentum tracks from the decay are usually well collimated; furthermore, the τ has a relatively long lifetime, so these tracks do not point to the vertex, but present non-zero impact parameter. This is defined as the distance of the track from the primary vertex; the transverse impact parameter is its projection orthogonally to the track direction). τ hadronic decays can, thus, be recognised because of the following characteristics:

- low track multiplicity, between one and three;
- narrow jet crossing the calorimeter;
- non-zero impact parameter.

Starting from these features, a likelihood function is built: by selecting the jets with a likelihood variable over a certain value, τ jets are isolated with a certain efficiency ϵ_τ, while the light jets are discarded with a certain rejection factor R_j. The precision of the algorithm increases with the energy, as the τ jets become narrower. Canonically, the efficiency is $\epsilon_\tau \sim 50\%$.

2.2.3. b-jets tagging

Hadrons containing b quarks decay a few mm far from the interaction vertex, differently from the ones containing light quarks only. The decay path of b-hadrons is measured through the impact parameter of the tracks originated in the decay: the distribution for

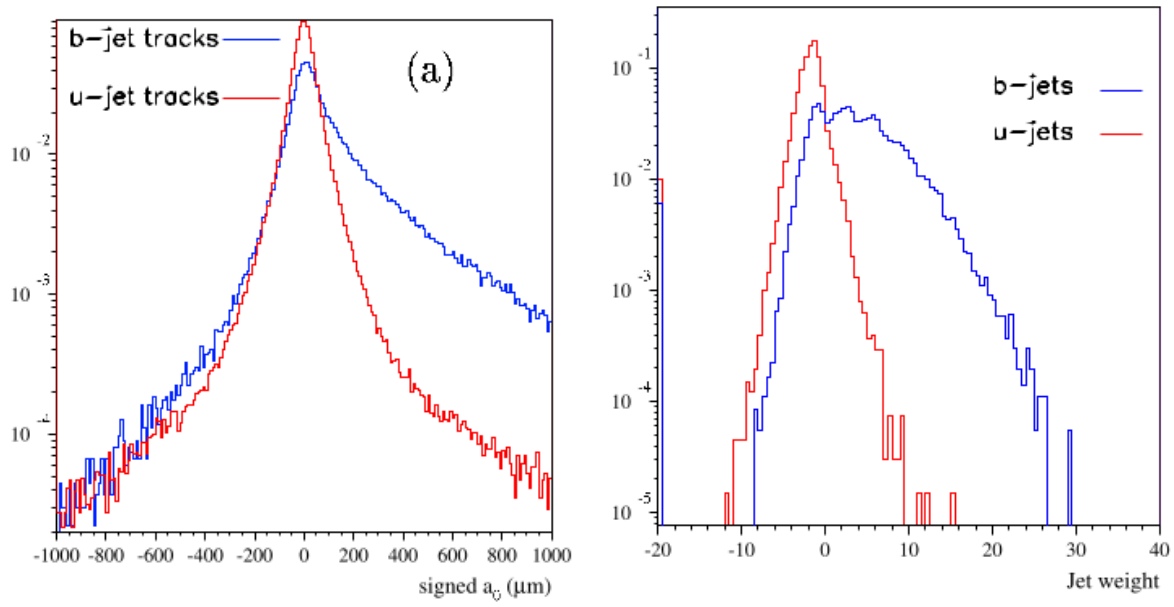

FIGURE 2.2.2. Typical transverse impact parameter and jet weight function for light jets (red) and b-jets (blue). They were obtained from samples of fully simulated WH, ttH, $\bar{t}t$ events, which have many b-jets in the final state[6]

light quarks is symmetric with respect to 0, while the one for b-hadron decays contains more positive values. This variable is more or less discriminant depending on the light quarks distribution width, which is related to the resolution of the pixel detectors layers near the beam line. An example of transverse impact parameter distributions for light and b-jets is shown in Fig. 2.2.2.
Each track in a jet is given a weight, based on its transverse impact parameter scaled by the intrinsic resolution: a jet weight function is built out of the product of these variables. An example of it, for light and b-jets, is reported in Fig. 2.2.2. The canonical efficiency for these jets is $\epsilon_b \sim 60\%$. Improvements can be obtained by considering the impact parameter component along the beam direction, and by looking for secondary vertexes inside the jets.

The main features of the most important LHC detectors are now presented.

2.2.4. ALICE

The Large Ion Collider Experiment is a heavy-ion detector which studies the strong interaction. The LHC generates collisions between Pb ions to recreate similar conditions than right after the Big Bang; protons and nuetrons free their quarks and gluons, which produce a plasma. ALICE studies this matter state as it cools down, observing how the particles we observe in the universe nowadays evolve. Many sub-detectors are present, to perform particle identification at different energies and with a high precision; in particular, the Time Projection Chamber (TPC) can give information on both particles trajectories and deposited energy. More details on the energy are provided by two electromagnetic calorimeters. ALICE is 26 m long, 16 m high, 16 m wide.

2.2.5. ATLAS

A Toroidal LHC ApparatuS investigates the physics beyond the Standard Model, at the highest energies reachable by the accelerator. It is divided in four layers: a Magnet system bends the charged particles trajectories, an Inner Detector measures their path, calorimeters identify photons, electrons and hadrons, and a spectrometer recognises muons. The electromagnetic calorimeter is placed in a 2 T toroidal magnetic field, while the hadronic ones are outside it. ATLAS is the largest volume particle detector ever built: it is 46 m long, 25 m high and 25 m wide.

2.2.6. CMS

The Compact Muon Solenoid spans from the Standard Model studies, to the search of dark matter and extra dimensions. It has the same purpose than the ATLAS detector, but the magnet system and the technques are different. The magnetic field is provided by a superconducting solenoid, that generates a 4 T field; it is confined by a steel armour. It is 21 m long, 15 m wide and 15 m high.

2.2.7. LHCb

The LHC beauty experiment analyses the differences between matter and antimatter through the study of the b quark. It measures the calues of the CKM matrix, in order to better understand the CP violation, related to the matter-antimatter concentration in the universe. A series of sub-detectors serve this purpose, one behind the other over a 20 m length: the vertex locator VELO, a first Ring Imaging Cherenkov, a magnet with three tracking stations, a second Ring Imaging Cherenkov, a scintillator, electromagnetic and hadronic calorimeters and some muon chambers. It is 21 m long, 100 m high and 13 m wide.

3. The SM as an Effective Field Theory

3.1. The need for new physics

The Standard Model has been very succesful so far in predicting particle properties and the reactions they undergo. Even when perturbation theory is no longer valid, as for strong interactions effects in low energy observables, tools have been implemented to obtain non-perturbative results. Despite this, we know the SM is not complete.
In its minimal version, it does not provide any mass term for the neutrinos. Completions for this have been proposed and some of them imply the presence of new degrees of freedom at high energy scales, around 10^9 - 10^{13} GeV[78].
Seondly, gravity is not contained the SM and lacks of a quantised formulation, so that the range of validity of the SM should not be larger than the Planck mass $M_{Pl} \approx 10^{19}$ GeV. This implies an amend near that scale, which is much larger than the ones we can reach at the LHC.
Moreover, it has been established that, if dark matter (DM) exists, no particle from the SM has all the properties required to be a candidate for it. The current cosmological model requires DM particles which are not too light and interact weakly with the SM states.
Another missing piece is the asymmetry between matter and antimatter that the universe presents: the SM cannot explain it completely unless new CP and baryon number violating dynamics are present[9].
Besides these reasons, some patterns within the SM itself suggest the presence of physics beyond the SM. As an example, the three SM gauge groups coupling constants evolve with energy and almost meet around 10^{14} - 10^{16} GeV, showing that they could originate from a larger group that is spontaneously broken at a higher scale. The simplest candidate is $SU(5)$, which would explain fermionic charge quantisation through quarks and leptons unification into multiplets, but unresolved issues are still present[10].
Then, radiative correction to some of the SM free parameters diverge quadratically, so that terms proportional to M_{Pl}^2 would appear. In order to end up with physical values of the Higgs mass and vacuum expectation value around the electroweak (EW) scale, fine-tunings of the bare parameters are required, but this is unacceptable for a renormalisable theory as the SM. This is called *hierarchy problem* and can be solved by new physics arising around the EW scale[11].
Another feature that is expected by new high-scale dynamics is to explain why there are three fermion generations in the SM, since no mechanism requiring this is known so far, nor gauge symmetries, renormalisability or gauge anomalies. For this reason, it is natural to consider some new physics process as responsible for these flavour structures.
Moreover, the SM forbids lepton (L) and baryon (B) numbers violation, but those global symmetries have been proved to be not fully reliable: non-perturbative effects have been shown to violate $U(1)_{B+L}$[12]. Since one of the simplest ways to introduce neutrino masses requires L to be violated by two units, B and L are expected not to be exactly respected; proton decay, however, puts very strong bounds on new sources of baryon number violation.

Given all these points, some new dynamics is expected to complete the SM at a certain scale.

3.2. Basics of EFT

An Effective Field Theory (EFT) is a simplification of a QFT, that zooms in a certain energy range.
It is a basic fact that Nature presents itself in many scales, from cosmology to particle ones, but it is also clear that, in order to describe physics at a given dimension, we do not need to know the dynamics at all of them. There are many examples of this: planetary orbital motions can be very well approximated even ignoring their internal compositions, and we can calculate the hydrogen atom spectum quite precisely by neglecting that protons and neutrons are made by quarks and gluons.
In particle physics, the relevant scales are the external masses and momenta and the collision energies. QFTs are used to make calculations, but this can be very challenging because of all the disparate dimensions that may be involved in the theory; not all of them, though, are probably relevant at the probed energy. This scale separation is formalized in the *Decoupling theorem* by Appelquist and Carazzone[13]: the effects of a *heavy* physics, characterized by a mass M, decouple at small momenta p, so that they only result in shifts of the low-energy renormalisation constants by factors of order $\mathcal{O}(p^2/M^2)$.
This is the EFT validity basis: the QFT of interest can be expanded in a series, up to an arbitrarily high order, around the energy we investigate. This means that we can take into account only the particles that are not too heavy to be produced at this energy, and integrate out all the other fields, which will contribute only through higher-order corrections:

$$\mathcal{L}_{full}\left(\phi_m, \phi_M\right) \approx \mathcal{L}_{full}\left(\phi_m\right) + \mathcal{L}_{EFT}\left(\phi_m, M^2\right). \tag{3.2.1}$$

The EFT Lagrangian can be written as a series of local operators O_i^d, each of them of a certain dimensionality d and weighted by its Wilson coefficient C_i:

$$\mathcal{L}_{EFT} = \sum_i \frac{C_i}{\Lambda^{d-4}} O_i^d \tag{3.2.2}$$

where Λ is a suppression factor, which can be thought as the characteristic scale of the new physics; its order of magnitude is the same as the mass M of the heavy fields which have been integrated out. For the EFT to be reliable, a gap has to exist among the energy p, probed in the experiment, and Λ: since we expect the corrections to this approximation to be proportional to some power of p^2/Λ^2, operators get more suppressed the higher their dimension, but only if there is a gap between p and Λ. This means that close to Λ, the full series would be needed to get precise enough results: for the EFT approximation up to a certain order to be useful, p does not have to be higher than some fraction of Λ. In this range, its predictions trustfully approximate the complete theory ones; outside this interval, though, they disagree, because the effects of the integrated-out fields become more important. The main idea, here, is that the terms in (3.2.2) encode the IR behaviour of fields and interactions inside the operators, while the UV dependency lies in the coefficients, which indeed can be fixed by requiring a matching of the results of both the EFT and the full theory, at the investigated energies.

As it can be seen by the generic expression (3.2.2), EFTs are not formally renormalisable, since they contain operators with a dimension greater than 4, in units of mass; the negative power of Λ they are multiplied by is, thus, needed to obtain the correct dimensionality for a Lagrangian term. An infinite number of counterterms are needed to cancel the divergent pieces at all orders, but it can be seen[14] that, if we stop at any given order in Λ, all the infinities can be reabsorbed with a finite number of terms: EFTs are order-by-order renormalisable in power counting. However, higher-dimensional operators provide power-like contributions to the amplitudes, which are function of the external momenta: this ends up with cross-sections that grow with energy below the scale Λ.
Given this, it is straightforward to summarise the steps for an EFT construction as[15]:

(1) Isolate and separate a series of characteristic scales in observables
(2) Expand the theory at the Lagrangian level, say build the EFT Lagrangian, as in (3.2.2), considering only the degrees of freedom (dofs) that are light enough to be produced. These may include propagating on-shell states, with a mass close to the process scale; for the more massive dofs, the propagator can be approximated as a constant
(3) Calculate in the EFT without any reference to the UV physics, which has been integrated out but is still present in the Wilson coefficients.

If loop calculations are involved, a mass-independent renormalisation scheme should be used, like dimensional regularisation, since this avoids power-like dependencies on unphysical scales, like a cut-off regulator, which could spoil the power counting and make it tricky.
As we have seen so far, EFTs are used to simplify calculations when not all the full theory scales are relevant for the investigated process: the Wilson coefficients in front of the operators can be derived explicitly by requiring for the IR predictions to be the same for both the hypotheses. The model-independency of EFTs, though, allows to apply them to all kinds of new physics research. In these cases, Λ is usually a fictitious scale, primarily introduced for dimensional reasons, with the only requirement for it to be larger than the involved energy scales, as a condition for the EFT validity. Furthermore, all the operators of a given dimensionality are in principle to be considered in the Lagrangian, since we do not know *a priori* what the UV theory is, and they can be mixed through renormalisation group (RG) equations[15]. Only symmetries can forbid some of them: we know that, in the SM, there are symmetries which alomost exact, up to a small breaking term, so if we force these symmetries to be unbroken in the EFT, the corresponding operators would remain suppressed. All the non-redundant operators at a certain dimension form a basis; the other ones are related to them through integration by parts, Fierz identities, equations of motion and field redefinitions[19]. All the Wilson coefficients of the basis have to be considered as free parameters, since no matching is possible without knowing the underlying theory. As a consequence, since both the coefficients and the Λ scale are unknown, we can only measure their ratio, for each operator, and then fix one of the two to test the validity of the result. For the EFT to be predictive, the expansion parameters have to be perturbative; since the coefficients are UV-dependent, this conditions implies bounds on the high-energy completion.
The EFTs can act as interfaces between the low energy phenomena we know and any heavy new physics we are theorising up to its mass scale, since the resonant production

of new theory's particle would spoil the predictions. The EFT we have been focusing on during this work is the Standard Model Effective Field Theory.

3.3. EFTs at colliders

EFTs are characterised by a huge number of free parameters, which cannot be usually fixed through matching operations, since the underlying theory is unknown. Data from colliders is used to set constraints on them, but since many operators contribute to more than one process, different observables have to be considered to distinguish them. One can take into account that, if a symmetry is preserved in the SM, the EFT parameters which violate it are usually numerically suppressed. In Minimal Flavour Violation (MFV), flavour symmetries are assumed to be exact and a breaking is put in a certain pattern, which is the same than the SM, to be sure it remains small[16]. The reduction of free terms that follows from this kind of assumptions enables a systematic EFT program using LHC data[15].
Examples of these IR assumptions are global symmetries like baryon or lepton number conservation or flavour symmetries; these lead to algebraic relations among scattering amplitudes and, hence, to constraints even if the symmetry is slightly broken. Since the IR limit is by definition reproduced by the EFT, these hypotheses are valid for many UV theories. If a certain flavour symmetry is assumed to be almost respected by the new physics, the EFT will feature the same approximate symmetry; the corrections remain small even at the loop order because of the symmetry. The symmetry assumptions can then be tested by adding the neglected operators.

3.4. The SMEFT

The SM is a great candidate for an EFT, since it is very well understood at the EW scale, but still a UV completion is needed, as it was shown in Sect. 3.1. In the SM Effective Field Theory (SMEFT), the idea is that some new state should be added to the SM, too heavy to be produced at the LHC, but interacting with the known states strongly enough to affect their interactions, which would show small deviations from the SM predictions.

3.4.1. Operator basis

At low energies, the action of these unknown heavy states is described through the addition of sets of higher-dimensional operators, which are built out of SM fields (which are summarised in Table 3.1, with their charges) but are $SU(3)_c \times SU(2)_L \times U(1)_Y$ singlets. These terms are suppressed by powers of a new physics scale Λ, whose value is *a priori* unknown, and can have different dimensionalities, depending on the order we want to stop at. The number of non-redundant operators is known from 5^{th} to 8^{th} order and a general algorithm has been implemented to determine bases even at higher orders, so that the SMEFT is defined at all orders in the local operators expansion[17]. In these terms, the Higgs is still considered as a $SU(2)_L$ doublet, since the measured properties of this particle indicate that it is SM-like. The lowest dimension term in the SMEFT is the unique dimension-five one

$$\mathcal{L}^{(5)} = \frac{C^{(5)}_{rs}}{\Lambda}\epsilon^{ij}\epsilon^{kl}\,(\ell^T_{ir}C\ell_{ks})H_jH_l + h.c. = \frac{C^{(5)}_{rs}}{\Lambda}\,(\widetilde{H}^\dagger\ell_r)^TC(\widetilde{H}^\dagger\ell_s) + h.c. \tag{3.4.1}$$

	$SU(3)_c$	$SU(2)_L$	$U(1)_Y$
$G^A_{\mu\nu}$	8	1	0
$W^I_{\mu\nu}$	1	3	0
$B_{\mu\nu}$	1	1	0
H	1	2	1/2
$q_r = (u^L_r, d^L_r)^T$	3	2	1/6
$\ell_r = (\nu^L_r, e^L_r)^T$	1	2	-1/2
$u_r = \{u_R, c_R, t_R\}$	3	1	2/3
$d_r = \{d_R, s_R, b_R\}$	3	1	-1/3
$e_r = \{e_R, \mu_R, \tau_R\}$	1	1	-1

TABLE 3.1. SM fields, with their charges[14]

with r, s flavour indices and i, j, k, l $SU(2)$ ones, C the charge conjugation matrix and $C^{(5)}$ the Wilson coefficient. This interaction violates the lepton number by 2 units ($\Delta L = 2$) and, when EW symmetry breaking occurs, provides a Majorana mass term for the neutrinos. Since these masses should be small, this operator is assumed to be generated at a very high scale. It can be shown[18] that operators constructed from the SM fields in Table 3.1 satisfy

$$\frac{1}{2}(\Delta B - \Delta L) = d \ \ (mod\, 2) \tag{3.4.2}$$

so an operator with dimension $d = 5$ cannot conserve both the baryonic and the lepton number.

The first basis for the 6^{th} order, which is the one this work is focused on, is known as the *Warsaw basis*[19]; its development took more than 20 years, from a first article[20] in 1986 and the final form published in 2010. Many attempts to remove redundant operators were performed over the years: starting from all the possible singlets under SM charges, there are many of them whose Wilson coefficients vanish when calculating observables. Relations among them can be established using equations of motion and Fierz identities, ending up with a basis of independent operators. There are 8 different classes, listed in Table 3.2 with the number of elements they contain, and their properties.

For one fermion generation, there are 59 $\Delta B = \Delta L = 0$ operators, some of which are Hermitian, with a real coefficient in the Lagrangian, while the non-Hermitian ones have a complex coefficient. Among these, 15 are bosonic operators, 19 are single-fermionic-current (mixed) ones and 25 lie inside the 4-fermion class; including the Hermitian conjugates, too, 76 operators are present for $n_g = 1$ fermionic generations, all of them in principle to be considered in the SMEFT Lagrangian with their coefficients.

The bosonic and mixed classes elements are listed in Table 3.3. The former ones are all Hermitian; those containing dual tensors $\widetilde{X}_{\mu\nu}$ are CP-odd, while the others are CP-even. For the mixed operators, Hermitian conjugation means transposing the generation indices for each fermionic current; the Hermitian conjugates are not listed in Table 3.3.

The counterterm structure of the 6^{th}-order SMEFT can be determined without expanding around the Higgs boson vev, as the scales introduced when this happens regulate the IR behaviour of the theory. Applying this approach, the dimension-six Warsaw basis was completely renormalised, using dimensional regularisation and the $\overline{MS}$ subtraction

	$n_g = 1$			$n_g = 3$		
	CP-even	CP-odd	Total	CP-even	CP-odd	Total
X^3	2	2	4	2	2	4
H^6	1	0	1	1	0	1
H^4D^2	2	0	2	2	0	2
X^2H^2	4	4	8	4	4	8
ψ^2H^3	3	3	6	27	27	54
ψ^2XH	8	8	16	72	72	144
ψ^2H^2D	8	1	9	51	30	81
$(\bar{L}L)(\bar{L}L)$	5	0	5	171	126	297
$(\bar{R}R)(\bar{R}R)$	7	0	7	255	195	450
$(\bar{L}L)(\bar{R}R)$	8	0	8	360	288	648
$(\bar{L}R)(\bar{R}L) + h.c.$	1	1	2	81	81	162
$(\bar{L}R)(\bar{L}R) + h.c.$	4	4	8	324	324	648

TABLE 3.2. Number of operators of each type at dimension-six in the SMEFT, where n_g is the number of fermion generations. X stands for $\{G^A_{\mu\nu}, W^I_{\mu\nu}, B_{\mu\nu}\}$, D for the covariant derivative and ψ for the fermionic fields. The classes containing the L doublets and the R singlets are called 4-fermion operators, while the previous ones are the bosonic and mixed operators[14]

X^3		H^6 and H^4D^2		ψ^2H^3	
O_G	$f_{ABC}G^{A,\nu}_\mu G^{B,\rho}_\nu G^{C,\mu}_\rho$	O_H	$(H^\dagger H)^3$	O_{eH}	$(H^\dagger H)(\ell_i e_j H)$
$O_{\widetilde{G}}$	$f_{ABC}\widetilde{G}^{A,\nu}_\mu G^{B,\rho}_\nu G^{C,\mu}_\rho$	$O_{H\Box}$	$(H^\dagger H)\Box(H^\dagger H)$	O_{uH}	$(H^\dagger H)(\bar{q}_i u_j \widetilde{H})$
O_W	$\epsilon_{IJK}W^{I,\nu}_\mu W^{J,\rho}_\nu W^{K,\mu}_\rho$	O_{HD}	$(H^\dagger D^\mu H)^*(H^\dagger D_\mu H)$	O_{dH}	$(H^\dagger H)(\bar{q}_i d_j H)$
$O_{\widetilde{W}}$	$\epsilon_{IJK}\widetilde{W}^{I,\nu}_\mu W^{J,\rho}_\nu W^{K,\mu}_\rho$				
X^2H^2		ψ^2XH		ψ^2H^2D	
O_{HG}	$H^\dagger H G^A_{\mu\nu}G^{\mu\nu}_A$	O_{eW}	$(\bar{\ell}_i\sigma^{\mu\nu}e_j)\tau_I H W^I_{\mu\nu}$	$O^{(1)}_{H\ell}$	$(H^\dagger i\overleftrightarrow{D}_\mu H)(\bar{\ell}_i\gamma^\mu\ell_j)$
$O_{H\widetilde{G}}$	$H^\dagger H \widetilde{G}^A_{\mu\nu}G^{\mu\nu}_A$	O_{eB}	$(\bar{\ell}_i\sigma^{\mu\nu}e_j)H B_{\mu\nu}$	$O^{(3)}_{H\ell}$	$(H^\dagger i\overleftrightarrow{D}^I_\mu H)(\bar{\ell}_i\tau_I\gamma^\mu\ell_j)$
O_{HW}	$H^\dagger H W^I_{\mu\nu}W^{\mu\nu}_I$	O_{uG}	$(\bar{q}_i\sigma^{\mu\nu}T_A u_j)\widetilde{H}G^A_{\mu\nu}$	O_{He}	$(H^\dagger i\overleftrightarrow{D}_\mu H)(\bar{e}_i\gamma^\mu e_j)$
$O_{H\widetilde{W}}$	$H^\dagger H \widetilde{W}^I_{\mu\nu}W^{\mu\nu}_I$	O_{uW}	$(\bar{q}_i\sigma^{\mu\nu}u_i)\tau_I\widetilde{H}W^I_{\mu\nu}$	$O^{(1)}_{Hq}$	$(H^\dagger i\overleftrightarrow{D}_\mu H)(\bar{q}_i\gamma^\mu q_j)$
O_{HB}	$H^\dagger H B_{\mu\nu}B^{\mu\nu}$	O_{uB}	$(\bar{q}_i\sigma^{\mu\nu}u_j)\widetilde{H}B_{\mu\nu}$	$O^{(3)}_{Hq}$	$(H^\dagger i\overleftrightarrow{D}^I_\mu H)(\bar{q}_i\tau_I\gamma^\mu q_j)$
$O_{H\widetilde{B}}$	$H^\dagger H \widetilde{B}_{\mu\nu}B^{\mu\nu}$	O_{dG}	$(\bar{q}_i\sigma^{\mu\nu}T_A d_j)H G^A_{\mu\nu}$	O_{Hu}	$(H^\dagger i\overleftrightarrow{D}_\mu H)(\bar{u}_i\gamma^\mu u_j)$
O_{HWB}	$H^\dagger\tau_I H W^I_{\mu\nu}B^{\mu\nu}$	O_{dW}	$(\bar{q}_i\sigma^{\mu\nu}d_j)\tau_I H W^I_{\mu\nu}$	Q_{Hd}	$(H^\dagger i\overleftrightarrow{D}_\mu H)(\bar{d}_i\gamma^\mu d_j)$
$O_{H\widetilde{W}B}$	$H^\dagger\tau_I H \widetilde{W}^I_{\mu\nu}B^{\mu\nu}$	O_{dB}	$(\bar{q}_i\sigma^{\mu\nu}d_j)H B_{\mu\nu}$	O_{Hud}	$i(\widetilde{H}^\dagger D_\mu H)(\bar{u}_i\gamma^\mu d_j)$

TABLE 3.3. Dimension-six bosonic operators in the Warsaw basis. Here, T^A matrices are normalised as $tr[T^AT^B] = \delta^{AB}/2$, while the τ^I fulfil $tr[\tau^I\tau^J] = 2\delta^{IJ}$; dual tensors are defined as $\widetilde{X}_{\mu\nu} = \frac{1}{2}\epsilon_{\mu\nu\rho\sigma}X^{\rho\sigma}$ and $\widetilde{H}^j = \epsilon_{jk}(H^k)^*$. The Hermitian counterparts, for the operators which have one, are not shown[19]. The fields are listed in Table 3.1

scheme: the basis closes at 1-loop and the 2499×2499 anomalous dimension matrix was completely determined[15]. The running of operators in $\mathcal{L}^{(6)}$ modifies the running of SM parameters, indicating that the field variables and operators are not independent, and related by the equations of motion. For this reason, it is not easy to translate the anomalous dimensions determined in the Warsaw basis to an alternate one: when removing operators to define it, the same equations of motion were used, requiring field redefinitions to be undone before changing the basis, and thus mapping the divergencies in the framework of an overcomplete theory. Only after that, another reduction to a non-redundant form has to be performed: only the Warsaw basis has been completely renormalised so far.

3.4.2. Progress and challenges

The SMEFT can be systematically probed through experiments.
Searches started concentrating on key processes for the SM, using final states that are not decayed and mapping them to SM; to improve the accuracy, the tails of the distributions and more differential measurements are investigated. In addition, low-energy observables can set constraints on the coefficients[21].
As the top quark is the known particle with the largest Yukawa coupling, it is the SM state which is closer to the new physics. In addition, it is less known because of its more recent discovery. It plays a fundamental role for the Higgs mass correction, being thus important for the understanding of the EW symmetry breaking in new models. This has motivated several analyses of the physics of this particle, based on the SMEFT approach. The LHC is currently producing a large top dataset. In the Warsaw basis, different operators directly involve this quark at dimension-six and other ones can be relevant for its processes, depending on the flavours and symmetries[15].
Each new operator added to the SM modifies the already known interactions, generates new vertices, or provides different energy dependencies to the existing ones. As an example, the *chromomagnetic moment* O_{tG}, whose expression is in Table 3.3, modifies the SM gtt coupling, since it introduces in the Lagrangian a term[24]

$$\mathcal{L}_{EFT} \supset \frac{2Re(C_{tG})v}{\sqrt{2}\Lambda^2}\,(\bar{t}\sigma^{\mu\nu}T^A t)G^A_{\mu\nu} + h.c. \tag{3.4.3}$$

where C_{tG} is the Wilson coefficient, v the Higgs vacuum expectation value and the T^A matrices are defined in Table 3.3. The modification of the gtt vertex induced by this operator is shown in Fig. 3.4.1, in the case of the Wt production process.

Each of these new interactions is an effective one, valid at low energies, of a more fundamental vertex in the underlying, unknown theory; but they may take part to different processes cross-sections, with a strength proportional to their coefficients. Thus, even if they are suppressed by powers of Λ, very precise measurements of the SM coupling constants should show hints of their presence, as small deviations from the SM predictions. In this work we will focus on the O_G operator, the first one of the X^3 class listed in Table 3.3, investigating the sensitivity to its interference with the SM and trying to understand its suppression.

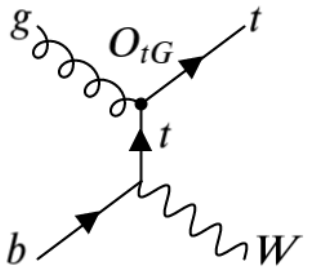

FIGURE 3.4.1. Modification of the SM gtt vertex due to the O_{tG} operator, in the case of the Wt production process. The dot differentiates the new interactions from the SM ones

3.5. The O_G operator

The triple-gluon operator is a CP-even, dimension-six element of the Warsaw basis, whose expression reads

$$O_G = g_s f_{ABC}\, G_\mu^{A,\nu} G_\nu^{B,\rho} G_\rho^{C,\mu} \tag{3.5.1}$$

with g_s the QCD coupling; it is made by the contraction of three gluon field strengths

$$G_{\mu\nu}^A = \partial_\mu G_\nu^A - \partial_\nu G_\mu^A + g_s f_{ABC}\, G_\mu^B G_\nu^C. \tag{3.5.2}$$

Once explicitly written, it can be seen that this term affects three and four gluon vertices, providing new energy dependencies, and generates additional interactions with five and six gluons. It can be generated at 1-loop by any coloured particle which interacts with the gluon field. It has a CP-violating counterpart $O_{\widetilde{G}}$, whose expression is displayed in Table 3.3, which starts to receive contributions at 2-loops and has been strictly constrained at low-energies[22]. On the other hand, the O_G provides contributions to dijet and multijet processes, even at tree-level, to scattering processes involving gluon self-interactions, and heavy quark production.
When added to the Lagrangian, the amplitudes of the processes it could take part to can be written as

$$\mathcal{M} = \mathcal{M}_{SM} + \mathcal{M}_{1/\Lambda^2} + \dots \tag{3.5.3}$$

where the first term contains the SM contribution and the Λ^{-2} term involves all the diagrams with one vertex from a dimension-six operator. The cross-sections of these processes can be written as expansion series around the SM ones, with the largest deviations given by the interference among this operator and the SM ($\mathcal{O}(\Lambda^{-2})$) and the square of $\mathcal{M}_{1/\Lambda^2}$ in the previous formula ($\mathcal{O}(\Lambda^{-4})$), as

$$\sigma = \sigma^{SM} + \frac{C_G}{\Lambda^2}\,\sigma^{1/\Lambda^2} + \left(\frac{C_G}{\Lambda^2}\right)^2 \sigma^{1/\Lambda^4} + \dots \tag{3.5.4}$$

In principle, other terms than $|\mathcal{M}_{1/\Lambda^2}|^2$ contribute to σ^{1/Λ^4}, like the interference between the SM and the diagrams with two vertices from O_G, through dimension-eight operators; in our case, though, we allow only one insertion of a dimension-six operator. The terms in (3.5.4) are the ones usually taken into account during measurements, but the dumping due to Λ powers make them hard to detect, with respect to the SM contribution.

It has been shown that the helicity structure of $2 \to 2$ processes, like $gg \to gg$ and $gq \to gq$, when involving this operator, is orthogonal to the pure QCD one, so that no interference is present at $\mathcal{O}(\Lambda^{-2})$ and non-zero contributions start at $\mathcal{O}(\Lambda^{-4})$[23]. For this reason, alternative processes are studied to constrain it, like multi-jet and heavy quark production ones. As an example, $gg \to t\bar{t}$ is an exception to this statement, since the $gg \to q\bar{q}$ interference is proportional to the quark mass; however, the color octet contribution to this process is small in the SM, so the constraints it provides are not very strong[24].
Recent studies[26] by Krauss, Kuttimalai and Plenh show that, despite the interference contribution is negligible in multijet production, terms of order $\mathcal{O}(\Lambda^{-4})$ and higher are important enough to be observed in high-energy events with many jets. These terms involve multiple insertions of vertices from dimension-six operators. In this article, multijet events are considered and the analysis is carried out through the observable

$$S_T = \sum_{j=1}^{N_{jets}} E_{T,j} + (\not{E}_T \ > \ 50\, GeV), \tag{3.5.5}$$

defined as the sum of the transverse energies of jets with p_T >50 GeV, plus any missing transverse energy over 50 GeV (the transverse energy is the energy of a jet calculated by considering only the projection of its three-momentum on the plane which is orthogonal to the beam axis). This variable distributions are shown in Fig. 3.5.1: it can be seen that they are quite accurately described by SM simulations, with any difference with the data inside the estimated uncertainties. The limit these histograms provide reads

$$\frac{C_G}{\Lambda^2} < (5.2\, TeV)^{-2} \tag{3.5.6}$$

with an integrated luminosity of 2.2 fb^{-1} at 13 TeV. They also took into account events with $S_T > \Lambda$, where the EFT validity is questionable, finding out that the bound is only mildly affected by this extension.

Further detailed analyses[25] showed that this is valid even when considering dimension-eight operators, whose expansion order in $1/\Lambda$ is the same than the squared dimension-six terms, and even when considering data from the highest energy region within the EFT validity range. The same article, by Hirschi, Maltoni, Tsinikos and Vryonidou, investigates the impact of the O_G over different jet observables. The results show that the $\mathcal{O}(\Lambda^{-4})$ contribution usually dominates the signal, while the interference intake is relevant only when considering a strength of the signal below the percent level. The same study also computed the next-to-leading order contribution of this operator to dijet processes in QCD, finding that interference contributions are present for 1-loop amplitudes including one O_G insertion, but they are too small with respect to the SM or even the $\mathcal{O}(\Lambda^{-4})$ ones.
The best constraint so far on the Wilson coefficient of the O_G has been determined through dijet measurements, using public data from the CMS experiment, by Goldouzian and Hildreth[27]. They consider the angular variable

$$\chi_{dijet} = e^{|y_1 - y_2|} \tag{3.5.7}$$

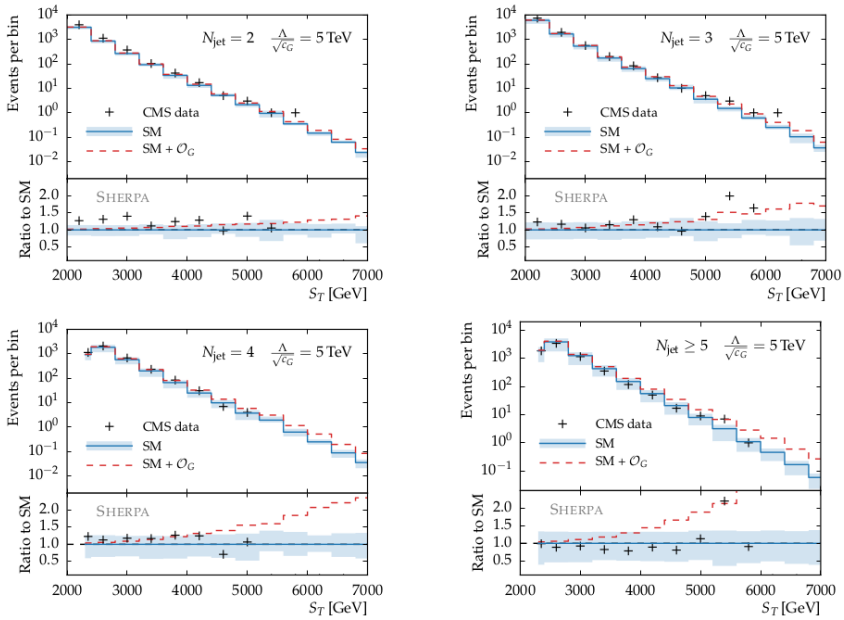

FIGURE 3.5.1. S_T distributions from CMS, in various bins of jet multiplicity N_{jets}, compared to signal and background predictions, including perturbative uncertainties[26]

with y_1 and y_2 the rapidities of the two highest energy jets among the detected ones. With CMS data at 13 TeV and an integrated luminosity of 35.9 fb^{-1}, normalised dijet angular distributions are measured over a wide range of dijet invariant masses. This shows that dijet angular distributions depend on the ratio of the O_G and SM cross-sections, σ_G/σ_{SM}, with the O_G contribution becoming more important at high masses. The bound this analysis imposes reads

$$\frac{C_G}{\Lambda^2} < (5.67\,TeV)^{-2} \tag{3.5.8}$$

at 95% confidence level (CL), which improves the already strong one of (3.5.6).
These results place a limit of $\Lambda \approx 5$ TeV on the UV scale, if assuming the C_G value to be close to 1.

4. Constraining the O_G operator

The target of this work is to revive the interference of the O_G operator with the SM. Good bounds on its Wilson coefficient C_G can already be imposed through the $\mathcal{O}(\Lambda^{-4})$ contribution; the interference is usually smaller in comparison, so our aim is to increase the sensitivity to it, as its sign is sensible to the coefficient one and the resulting constraints on Λ will improve faster than those of from the Λ^{-4} order.
The Monte Carlo generator we use, Madgraph@NLO[32], can simulate events for the full model, containing in the matrix element the pure SM contribution, the squared amplitude of the diagrams with one dimension-six operator in one vertex and the interference between these two. This last term, contrarily to the previous ones, is not positive-definite. Even events for each separate contribution can be generated. In each of these cases, a weight is assigned to every event; all the weights of the $\mathcal{O}(\Lambda^{-2})$ interference sample have the same absolute value, but different sign depending on the sign of the event matrix element. As a consequence, when the interference events are added to the SM and $\mathcal{O}(\Lambda^{-4})$ ones, the cross-section is increased when the interference is positive and decreased when it is negative.
The idea behind this work is that the suppression of the interference contribution to the total cross-section is due to a sum over different phase space regions, in each of which there are more positive- or more negative-weighted events. This would imply that, even if the interference cross-section is almost null, if compared to the SM and $\mathcal{O}(\Lambda^{-4})$ ones, it is non-zero over different phase space zones, but it changes of sign between those.

In Table 4.1 and 4.2 respectively, the interference and the SM cross-sections for the processes which are sensitive to the O_G operator are displayed, with the percentage of positive-weighted events in the generated interference samples. It can be seen that, for the top-pair production, there is no such cancellation over the phase space; for $pp > t\bar{t}j$, even if the cancellation is bigger than for top pair production, the cross-section and the cancellation are smaller than for the multi-jet processes; finally, three-jet production is easier to handle than the four-jet one, because of the smaller number of involved subprocesses and the simpler kinematics, and the cancellation between positive- and

	$p_T > 50$ GeV		$p_T > 200$ GeV		$p_T > 1000$ GeV	
process	σ [pb]	wgt>0	σ [pb]	wgt>0	σ [pb]	wgt>0
$pp > t\bar{t}$	1.388	85.0%	1.384	85.2%	1.384	85.1%
$pp > t\bar{t}j$	$5.20{\cdot}10^{-1}$	62.4%	$1.13{\cdot}10^{-1}$	60.4%	$1.37{\cdot}10^{-3}$	62.0%
$pp > jjj$	$2.98{\cdot}10^{1}$	51.6%	$5.90{\cdot}10^{-1}$	52.4%	$4.91{\cdot}10^{-4}$	61.2%
$pp > jjjj$	$-2.89{\cdot}10^{1}$	45.4%	$-2.50{\cdot}10^{-1}$	44.2%	$-4.12{\cdot}10^{-6}$	38.8%

TABLE 4.1. $\mathcal{O}(\Lambda^{-2})$ cross-section and percentage of positive-weighted events for some processes which have been proved to show a non-null interference between the SM and the O_G operator. These results are calculated for $\Delta R > 0.4$ and different minimum values for the transverse momentum p_T (see Sect. 4.1 for the definitions of the last two)

process	$p_T > 50$ GeV	$p_T > 200$ GeV	$p_T > 1000$ GeV
$pp > t\bar{t}$	$5.20{\cdot}10^2$	$5.18{\cdot}10^2$	$5.18{\cdot}10^2$
$pp > t\bar{t}j$	$2.67{\cdot}10^2$	$3.10{\cdot}10^1$	$4.82{\cdot}10^{-2}$
$pp > jjj$	$1.20{\cdot}10^6$	$1.06{\cdot}10^3$	$1.10{\cdot}10^{-2}$
$pp > jjjj$	$1.95{\cdot}10^5$	$7.15{\cdot}10^1$	$5.96{\cdot}10^{-5}$

TABLE 4.2. SM cross-section, in [pb], for the same processes in Table 4.1. These results are calculated for $\Delta R > 0.4$ and different minimum values for the transverse momentum p_T (see Sect. 4.1 for the definitions of the last two)

negative-weighted events is bigger in the three-jet case. Moreover, the three-jet cross-section is larger, so that they are more suitable for differential measurements. For these reasons, we concentrate on three-jet production: events of this kind are generated through Monte Carlo simulations and different variables are calculated for each of them and, then, plotted. The idea is to select some observables which are relatively easy to measure at colliders and that can divide well enough the events with positive and negative matrix elements contributing to the interference cross-section; those are then used to set bounds on the C_G coefficient.

4.1. Some definitions

In this analysis, we consider the two incoming particles to move along opposite directions on the z axis, which we call the *beam axis*. In the following, the three-vector quantities are written in bold characters. For any outgoing jet, we name θ the angle between the beam axis and its three-momentum $\boldsymbol{p}$, so that its pseudorapidity can be expressed as

$$\eta = -\log\left(\tan\frac{\theta}{2}\right). \tag{4.1.1}$$

We call the *transverse momentum* $\boldsymbol{p_T}$ the projection of $\boldsymbol{p}$ on the xy plane, orthogonal to the beam direction. Using ϕ to indicate the angle among $\boldsymbol{p_T}$ and the y axis, we can build the angular distance between two jets as

$$\Delta R = \sqrt{(\eta_2 - \eta_1)^2 + (\phi_2 - \phi_1)^2}. \tag{4.1.2}$$

The angles and the transverse momentum are represented, for one jet, in Figure 4.1.1. If we name $\hat{\boldsymbol{n}}_{\boldsymbol{T}}$ the unit vector that maximises the sum of the projections of the outgoing transverse momenta $\boldsymbol{p_{T,i}}$ over itself, we can divide the orthogonal plane in an upper region $\mathcal{C}_U$, including all the jets with $\boldsymbol{p_T} \cdot \hat{\boldsymbol{n}}_{\boldsymbol{T}} > 0$, and a lower one $\mathcal{C}_L$, where $\boldsymbol{p_T} \cdot \hat{\boldsymbol{n}}_{\boldsymbol{T}} < 0$. The $\hat{\boldsymbol{n}}_{\boldsymbol{T}}$ can be defined only up to an overall sign, but changing that would only exchange the two sides. Given this, we can define the pseudorapidities and the azimuthal angles for the upper and lower regions as

$$\eta_X = \frac{\sum_{i\in\mathcal{C}_X} p_{T,i}\eta_i}{\sum_{i\in\mathcal{C}_X} p_{T,i}}, \qquad \phi_X = \frac{\sum_{i\in\mathcal{C}_X} p_{T,i}\phi_i}{\sum_{i\in\mathcal{C}_X} p_{T,i}} \tag{4.1.3}$$

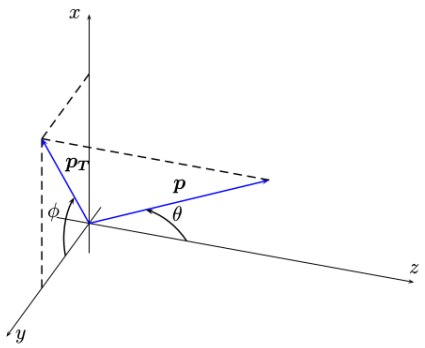

FIGURE 4.1.1. Some quantities used in jet analysis. The incoming beams travel along the z direction, while $\boldsymbol{p}$ is the momentum of one outgoing jet

where X stands for U or L sides and the sums are scalar ones. In both these regions, we define the *jet broadening* variable as

$$B_X = \frac{1}{2\sum_{i\in\mathcal{C}_X} p_{T,i}} \sum_{i\in\mathcal{C}_X} \sqrt{(\eta_i - \eta_X)^2 + (\phi_i - \phi_X)^2} \tag{4.1.4}$$

and the total jet broadening is $B_{tot} = B_U + B_L$[28].
The event *transverse thrust* observable is defined as

$$\tau_\perp = 1 - \frac{\sum_i |\boldsymbol{p_{T,i}} \cdot \hat{\boldsymbol{n}}_{\boldsymbol{T}}|}{\sum_i p_{T,i}}. \tag{4.1.5}$$

This is sensitive to the jets topology: it is valued 0 for perfectly balanced two-jet events, while it amounts to $(1 - 2/\pi)$ for isotropic multijet events[28].

4.2. The procedure

4.2.1. Generating the samples

We use the TopEffTh[29] Universal FeynRules Output (UFO)[30], written from a FeynRules model[31] containing the dimension-six operators in the Warsaw basis. This is then submitted to the Madgraph@NLO Monte Carlo generator.
The considered process is the three-jet production $pp \to jjj$ from the collision of two partons, as we discussed above, with all the operators coefficients but the O_G one set to 0; three samples with 100000 events each are created for the SM, the $\mathcal{O}(\Lambda^{-2})$ interference and the $\mathcal{O}(\Lambda^{-4})$ new physics contributions at leading order (LO), with up to one insertion of the O_G in the diagrams. The Parton Distribution Fuction (PDF) we use is the NNPDF2.3. The u, d, c, s quarks masses are neglected: this is referred as *four-flavour scheme*. Furthermore, we have checked that the QED-like processes contribute for less than the 1% to the cross-sections, so they are not taken into account, in order to speed up the calculations.
For each sample, we set $|\eta| < 5$, $\Delta R > 0.4$ and considered different lower cuts on the transverse momentum of all the jets, namely 50, 100, 200, 500 and 1000 GeV. These last two cuts are needed to avoid divergencies in gluon propagators: if a gluon splits in other two real ones with momenta p_1 and p_2, and these two are too close in space to each other, then its propagator would present at denominator a factor $p^2 \approx (2p_1)^2 = 0$,

which would lead to a divergence. An analogous problem would show up for too small values of the transverse momenta for the particles: for these reasons, minimum values are imposed on them in the simulations.
In order to avoid the introduction of an event-by-event renormalisation, a fixed scale is set for all the events: at 150 GeV for p_T >50 GeV, at 250 Gev for p_T >100 GeV, at 500 GeV for p_T >200 GeV, at 1000 GeV for p_T >500 GeV and at 2000 GeV for p_T >1000 GeV.

4.2.2. Choosing the variables

The best discriminant to separate the positive- and neative-weighted regions is the matrix element[33] of the interference, as its sign is the same than the weight of the event it is calculated from. However, this is difficult to compute for partonic events, and even more for real ones: it depends on the momenta of the involved particles, the flavours and the helicities of the partons, but the only information which are experimentally available among these are the momenta of the final jets. We are, thus, looking for variables which are simpler to measure and that can discriminate the differently weighted phase space regions with their value: in this way, by imposing cuts on these quantities, it would be possible to isolate quite well the zones in which the interference differential cross-section has a certain sign.
Once the interference events are stored, different variables are estimated for each of them and plotted in differential cross-section histograms, separating the values that come from positive-weighted events and the ones obtained by negative-weighted ones. The distributions we have considered are:

- the transverse momenta of the jets
- the pseudorapidity of the jets, defined in (4.1.1)
- the invariant masses of the jets, in pairs of 2 and all together
- the angular distance between pair of jets, defined in (4.1.2)
- the normalised triple product of the three-momenta of the jets, $\frac{(\boldsymbol{p_1}\times\boldsymbol{p_2})\cdot\boldsymbol{p_3}}{|\boldsymbol{p_1}\times\boldsymbol{p_2}||\boldsymbol{p_3}|}$ and permutations of the indices; the numerator does not change for cyclic changes, but the denominator does
- the total jet broadening of the jets, defined in (4.1.4)
- the event transverse thrust, as it is defined in (4.1.5)
- some double differential distributions, involving pairs of the above quantities; these allow to consider dynamical features from all the jets in one plot, and not by taking them in pairs as for many of the above observables.

The *good variables* that we are searching are the ones whose distributions present regions with more positive weights and regions with more negative ones. They allow to divide these two zones quite accurately by simply considering only the events for which those particular observables have values above or below one or more cuts. As a result, the cross-sections on these parts of the phase space almost cancel each other, having different signs, ending up in the almost vanishing contribution of the interference to the total cross-section mentioned above. This behaviour suggests these variables to be sensitive to the action of O_G and makes them good candidates to set bounds on its Wilson coefficient.
In the case of the double differential distributions, the interesting ones can actually

divide the negative and positive cross-section zones by isolating compact intervals of the two involved observables: they have to show connected regions with more positive than negative weights and viceversa, over the two-variables plane.

4.2.3. The χ^2 distribution

Given one of these promising differential cross-section distributions, we can build out of it a χ^2 function

$$\chi^2 = \sum_i \left(\frac{x_i^{exp} - x_i^{th}}{\Delta_i} \right)^2 \tag{4.2.1}$$

which quantifies the difference between the experimental data and the SM+$\mathcal{O}(\Lambda^{-2})$ + $\mathcal{O}(\Lambda^{-4})$ theory; since we do not have the former, we consider it to be the variable distribution over the pure SM sample. In the formula above, the sum is performed over all the bins of the histograms, with x_i their contents: we are, in theory, bin-per-bin subtracting from the differential cross-sections in the variable distribution over the SM sample, the ones in the distribution of the same variable over the SM + O_G theory. In practice, the SM contributions cancel off with each other, so that we can consider the interference and new physics data only to calculate the observable distribution and sum over it. The Δ_i at the denominator of (4.2.2) represents the error over the i^{th} bin: it has to contain uncertainties from PDFs and scale variations, but also experimental errors. According to reference[34], we consider it as 10% of the content of the respective bin in the SM distribution. This is, however, only an estimation and only furnishes its order of magnitude; since we are analysing some simulations, we do not have experimental uncertainties to involve, while they would be taken into account when studying real data.
Considering the experimental data as the SM distribution and stopping at the interference order, the χ^2 formula reduces to

$$\chi^2 = \sum_i \left(\frac{\frac{C_G}{\Lambda^2}\sigma_i^{1/\Lambda^2}}{\Delta_i} \right)^2 . \tag{4.2.2}$$

The only unknown quantity in (4.2.2) is the ratio C_G/Λ^2, common to all the terms in the summation. Thus, we can put bounds on it by choosing a confidence level and imposing the χ^2 of equation (4.2.2) to reamin in that interval. It is easy to see that (4.2.2) has its minimum for $C_G = 0$, since we are considering the deviations of the theory from the SM, but real measurements should observe a non-null minimum, even if near 0. For this reason, for what concerns our simulation, the closer the bounds are to 0, the better this procedure would work to constrain the C_G value, once experimental data are provided.
The χ^2 functions varies with the chosen binning for the variable distributions. Since the SM, the interference and the new physics contributions are all needed to compute it (the SM one determines the errors at the denominator), we set the same interval division for all of them. The binnings are chosen in order to guarantee the 10% accuracy with respect to the SM plots: since the tails of the distributions usually contain a smaller event quantity, a large bin is put at the end of the interference histograms, when the number of events in their last bins is not sufficient to ensure a 10% statistical uncertainty. These numbers of events are calculated, from the differential cross-section in each bin, by considering a luminosity of 100 fb^{-1}, which is the order of magnitude of the Run II

luminosity at the LHC[35]. For the transverse momenta, a large last bin is however applied to the distributions, as the validity of the EFT decreases as the energy increases: above a certain limit, its previsions are no more fully reliable.
In order to check the effect of higher order corrections, one can include in (4.2.2) the $\mathcal{O}(\Lambda^{-4})$ contribution, namely the variable distribution over the new physics sample. This would reshape the χ^2 as

$$\chi^2 = \sum_i \left(\frac{x_i^{exp} - x_i^{th}}{\Delta_i} \right)^2 = \sum_i \left(\frac{\frac{C_G}{\Lambda^2}\sigma_i^{1/\Lambda^2} + \frac{C_G^2}{\Lambda^4}\sigma_i^{1/\Lambda^4}}{\Delta_i} \right)^2 . \tag{4.2.3}$$

Once developed the square, a 3^{rd} and a 4^{th} order terms in C_G/Λ^2 appear besides the already present 2^{nd} order one, giving the function an asymmetric trend with respect to the minimum in 0: this implies different lower and upper bounds on the Wilson coefficient. The procedure to obtain them, though, is the same than before.
These χ^2 functions can be calculated even over double differential distributions: the sum is then performed over all the rectangular bins on the two-variable plane and bounds on the C_G are assigned as above. Since most of the considered single-variable distributions involve one or two jets per time, this is a way to obtain dynamical information from all the jets in one plot, i.e. by considering the ΔR between two pairs of outgoing particles: this allows to use details from the entire event to constrain the coefficient. Moreover, it helps finding out the correlation among the variables: the more the two observables are dependent from each other, the more their double differential plot would show the events with the same weight closer to a straight diagonal line, whose slope depends on the kind of proportionality. This kind of plots, thus, also throws light on which variables are more interesting than others in constraining the C_G value.

4.3. Results

In the following, the jets will be ordered from the 1^{st} to the last one by decreasing module of the transverse momentum, p_T.
The cross-sections for the three-jet production, including all the different orders in Λ^{-1} and each p_T-cut, with up to one insertion of the O_G, are summarised in Table 4.3; for the interference, the positive weight percentages and the sum of the absolute values of the weights are displayed, too. It can be seen that a low cut on the p_T implies larger cross-sections, but also a less important contribution, compared to the SM, from the O_G, which begins to be relevant at higher energies; on the other side, an high cut provides too small cross-sections and a smaller cancellation between positive- and negative-weighted events. For these reasons, we mostly concentrate on the p_T >200 GeV events, as a trade-off between these features: this allows to consider different variable distributions and guarantees the new physics not to be completely negligible with respect to the SM. Furthermore, the percentage of positive-weighted events shows that the cancellation is not so complete for an high p_T-cut, so that those regions are less interesting to revive the interference.
Both the $\mathcal{O}(\Lambda^{-2})$ and the $\mathcal{O}(\Lambda^{-4})$ contributions are by orders of magnitude smaller than the SM one; moreover, the interference is suppressed even with respect to the new physics interactions, and this is due to the O_G operator nature and the cancellation it generates

	SM	$\mathcal{O}(1/\Lambda^2)$			$\mathcal{O}(1/\Lambda^4)$
$p_{T,min}$ [GeV]	σ [pb]	σ [pb]	wgt>0	$\sum$|wgt|/events [pb]	σ [pb]
50	$5.29{\cdot}10^{5}$	2.77	50.1%	$6.06{\cdot}10^{2}$	$2.24{\cdot}10^{1}$
100	$2.53{\cdot}10^{4}$	1.17	50.7%	$1.02{\cdot}10^{2}$	9.20
200	$8.94{\cdot}10^{2}$	$2.98{\cdot}10^{-1}$	51.2%	$1.25{\cdot}10^{1}$	2.73
500	4.72	$2.29{\cdot}10^{-2}$	53.4%	$3.28{\cdot}10^{-1}$	$2.16{\cdot}10^{-1}$
1000	$2.21{\cdot}10^{-2}$	$9.47{\cdot}10^{-4}$	59.3%	$5.13{\cdot}10^{-3}$	$6.86{\cdot}10^{-3}$

TABLE 4.3. Cross-sections for three-jet production, for different values of the p_T-cut, $\Delta R > 0.4$, $\Lambda = 5$ TeV and renormalisation scales fixed respectively at 150, 250, 500, 1000 and 2000 GeV, with up to one O_G insertion. The percentages of positive-weighted events are shown for the interference; the relative errors over these percentages are around the 0.3%. The sum of the absolute values of the event weights, normalised to the total number of events, is reported for the interference

over the phase space: this suppression holds for any p_T-cut.
The promising variable distributions we found, calculated over the interference events, are shown in Fig. 4.3.1, for $p_T > 200$ GeV; the used binnings are described in Table 4.4. These quantities are the transverse momentum of the 1^{st} jet $p_T[j_1]$, the angular distance between the 2^{nd} and 3^{rd} jets $\Delta R[j_2 j_3]$, the absolute value of the pseudorapidity of the 3^{rd} jet $|\eta[j_3]|$, the normalised triple product of the momenta of the three jets $|(\boldsymbol{p_1} \times \boldsymbol{p_2}) \cdot \boldsymbol{p_3}|/(|\boldsymbol{p_1} \times \boldsymbol{p_2}||\boldsymbol{p_3}|)$, the total jet broadening and the transverse thrust. In these histograms, each coloumn represents the differential cross-section for each bin into which the variable range is divided: the red coloumns are the contributions from positive-weighted events, the blue ones are from the negative-weighted ones. Their difference, which shows the total differential cross-section distribution for the interference, is summarised by the green line: since it presents a change in sign for certain values of these observables, an almost complete cancellation occurs over the full range. By considering these plots, it is straightforward to separate the phase space regions that contribute positively on top of the SM cross-section and the ones that are decreasing it, by just putting a cut on one of these variables near the sign flip. These distributions show similar features for all the p_T-cuts.
Some examples of quantities not worth to consider are shown in Fig. 4.3.2, calculated over the interference sample with the p_T-cut at 200 GeV: it is possible to see that the positive- and negative-weighted events lead to almost the same distribution, so that their difference, which is the differential cross-section distribution of the interference, vanishes pretty much everywhere. As a consequence, no possibility exists to isolate the differently contributing phase space regions by discriminating the events with respect to these variables.
Some examples of double differential distributions are reported in Fig. 4.3.3. As for the previous ones, the binnings are described in Table 4.4; they can be different from the single distributions ones, in order to have a similar number of bins for all the histograms. In these histograms, the total differential cross-section in each bin is valued through colors, which are codified in legends besides each plot; red shades are used for

positive values and blue shades for the negative ones. Analogously to single distribution plots, the promising ones are like the first two in the figure, namely $p_T[j_1]$ vs $\Delta R[j_2 j_3]$ and $p_T[j_1]$ vs $|(\boldsymbol{p_1} \times \boldsymbol{p_2}) \cdot \boldsymbol{p_3}|/(|\boldsymbol{p_1} \times \boldsymbol{p_2}||\boldsymbol{p_3}|)$: one can isolate the red and blue zones quite well by putting cuts on both varibles simoultaneously. This does not happen for the third example in Fig. 4.3.3, since the cross-section values seem not to be correlated to the value of the 1^{st} jet pseudorapidity: no cut on that variable can discriminate the phase space regions. These features are somehow espected, since in the first two cases we are plotting together pairs of variables we already tagged as *good* ones, by inspecting their single distributions in Fig. 4.3.1, while in the third example we are involving one quantity for which the interference cross-section is null almost everywhere in the single-variable plot. The double differential distributions of $p_T[j_1]$ vs $p_T[j_3]$, $\Delta R[j_2 j_3]$ and $\Delta R[j_1 j_3]$, in Fig. 4.3.3, suggest that the sign change is related to the topology of the events: events with three well separated and balanced jets contribute with an opposite sign than the events that are more dijet-like.

Given these distributions, we calculate the χ^2 functions over them, using formulas (4.2.2) and (4.2.3); these involve the SM and pure new physics differential cross-section distributions, which are not shown here because they are always positive, and no cancellation occurs. We consider, for each variable, a number of dofs which is one less than the quantity of bins in its histogram, since the C_G coefficient is the only free parameter present. Then, we recover from tables the critical value of the χ^2 distribution at 68% CL, for the specific number of dofs, and we impose our functions (4.2.2) and (4.2.3) to satisfy it: this provides us bounds on the value of C_G, the only unknown quantity in those expressions as we set $\Lambda = 1$ TeV. The results are summarised in Table 4.5, the ones up to $\mathcal{O}(\Lambda^{-2})$ order first, and the ones up to $\mathcal{O}(\Lambda^{-4})$ in brackets.

As expected, the C_G is more constrained by the $\mathcal{O}(\Lambda^{-4})$ contribution, partially because of the cancellation the $\mathcal{O}(\Lambda^{-2})$ order undergoes, but also because the $\mathcal{O}(\Lambda^{-4})$ distributions differ more from the SM ones than the interference. At the interference order, anyway, good bounds come from the double differential distributions, which have been taken into account to consider features from all the jets in the events. Among the single distributions, the 1^{st} jet transverse momentum, the angular distance between the 2^{nd} and 3^{rd} jets and the transverse thrust give the stronger constraints: the last one involves all the jets directly as the previous ones, while the previous ones are not strictly linked to the topology of the entire events, but are somehow correlated, since the higher the p_T of one jet, the closer in space have to be the other two to compensate. For the p_T of the 1^{st} jet, the results from two different binnings are used, to show the impact of this on the bounds: it can be seen that refining the binning of a factor 2 improves the constraints of about 10%. Therefore, even if not all the distributions have the same number of bins, we can compare their results, as they would change slightly with a different binning.

The limits from the distributions which do not show any significant sign flip at interference order are much worse than the other ones, as it can be seen from the pseudorapidity of the first jet in Table 4.5.

In Fig. 4.3.4, the bound on C_G is displayed, as a function of the upper cut over the center-of-mass energy ($\sqrt{s}$), for $\Lambda = 1$ TeV and considering the $p_T[j_1]$ distribution with

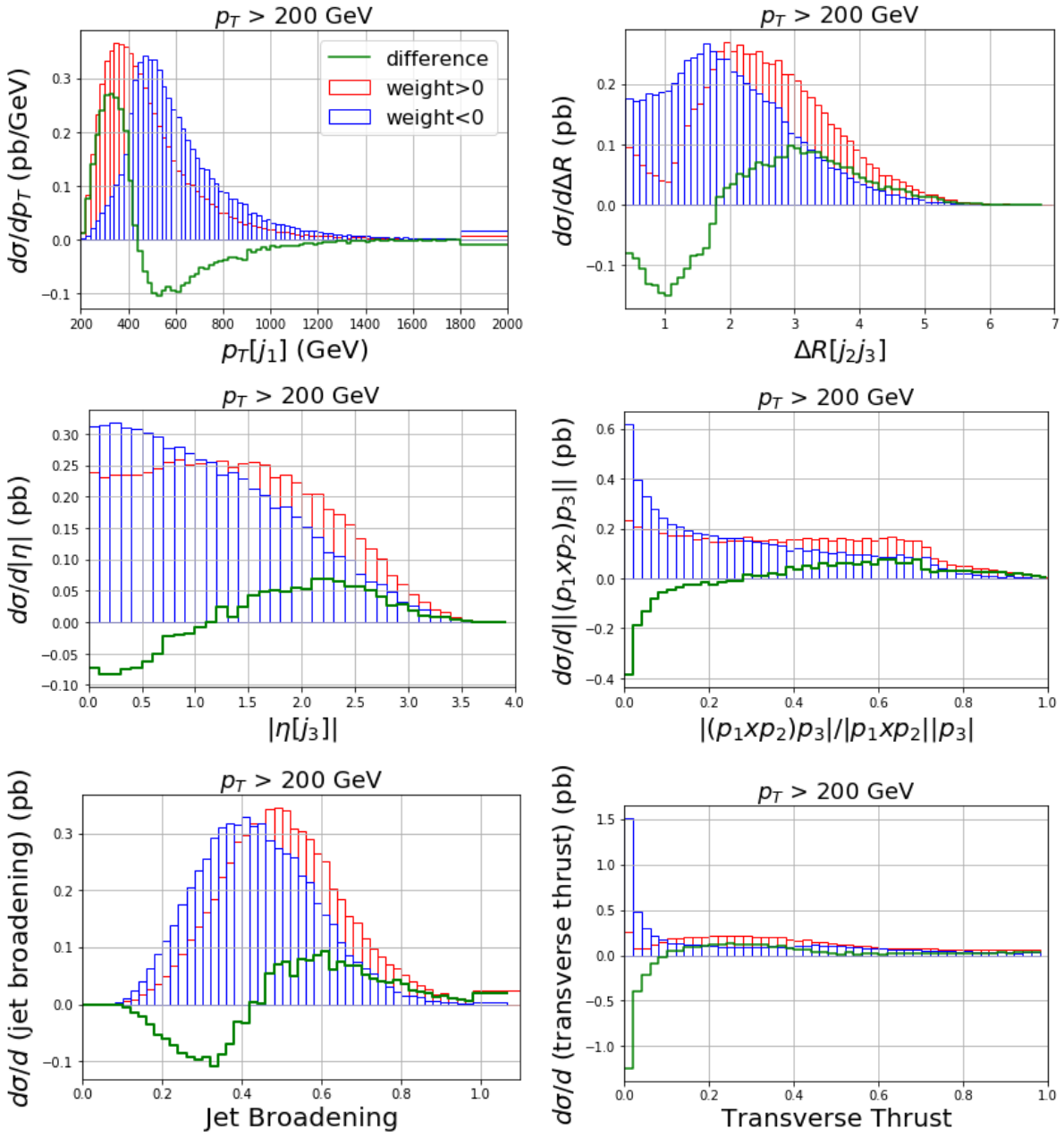

FIGURE 4.3.1. Examples of differential distributions that better divide the interference events, for $p_T > 200$ GeV; respectively, the transverse momentum of the 1^{st} jet, the angular distance between the 2^{nd} and 3^{rd} jets, the pseudorapidity of the 3^{rd} jet, the triple product of the momenta of the three jets, the jet broadening and the transverse thrust. The red line represents the differential cross-section contribution by the positive-weighted events, the blue one the income from negative-weighted ones; their difference, the green plot, is the differential cross-section distribution for the interference. All of them show one or more sign flips in the differential cross-section trend, for certain values of the observable. The relative binnings are described in Table 4.4; for the transverse momentum and the jet broadening, the last bin is not entirely shown

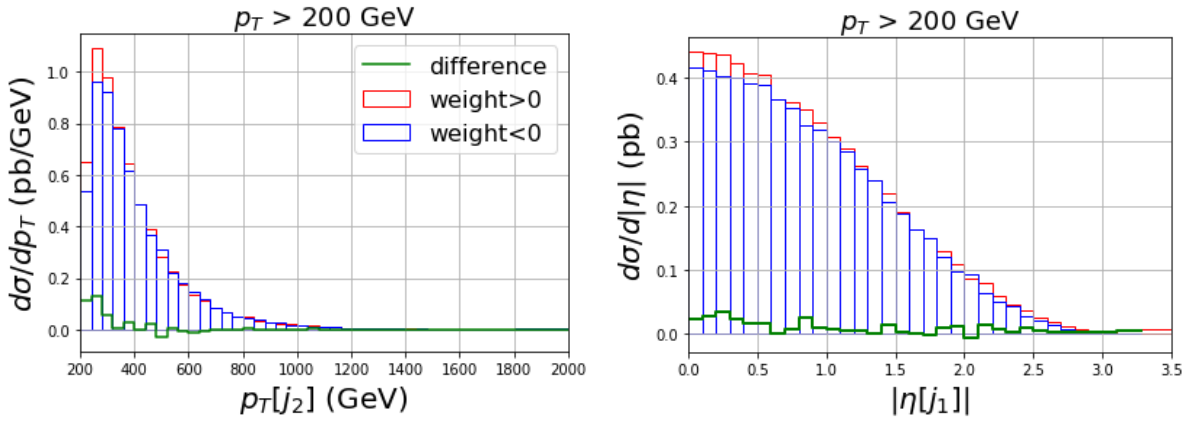

FIGURE 4.3.2. Some examples of differential distributions that do not divide the interference events, for $p_T > 200$ GeV; respectively, the transverse momentum of the 2^{nd} jet and the pseudorapidity of the 1^{st} jet. The red line represents the differential cross-section contribution by the positive-weighted events, the blue one the income from negative-weighted ones; their difference is the green plot. The cross-section is almost null all over the range, so that an analysis of the interference effects is not worth it. The relative binnings are described in Table 4.4; for both the distributions, the last bin is not entirely displayed

bins of 40 GeV. The red plot takes into account the interference only, as the χ^2 is calculated through (4.2.2), while the blue plots consider the $\mathcal{O}(\Lambda^{-4})$ order too, as they come from a χ^2 computed as in (4.2.3). Only the upper bound is shown for the interference, as the lower one is symmetric with respect to the horizontal axis. The green line shows the bound obtained by all the events, as it is reported at the first line of Table 4.5. Above 3.5 TeV, curves are flattening out, showing that events above that energy do not play a major role in constraining the C_G value; with such a cut, the constraints are valid as for new physics scale above roughly 5 TeV. Below these energies, the interference-only curve decreases faster than the other one, as expected from their different dependence in the C_G/Λ^2 coefficient, i.e. linear versus quadratic.
In Fig. 4.3.5, the upper bounds on the new physics scale, Λ, as functions of the cut over the center-of-mass energy are shown, calculated by considering $C_G = 1$. These results are inferred from the $p_T[j_1]$ distribution, the one with bins of 40 GeV. The red plot takes into account the interference only, while the blue plot considers the $\mathcal{O}(\Lambda^{-4})$ order too. The green line displays the bound obtained using all the events, with no cut on $\sqrt{s}$. Similarly as for the previous figure, it can be seen that the the bound from the interference increases faster than the one from the $\mathcal{O}(\Lambda^{-4})$ contribution, as expected due to their difference dependence on Λ. As the cut becomes stronger, both curves flatten off, showing that the last few events at high energy do not add much information.

4.4. Matrix element check

The main feature the variables have to fulfil to be taken into account for this analysis, is to be able to discriminate the positive- and negative-weight regions of the phase space. The best way to do this is through the interference matrix element, as it has the

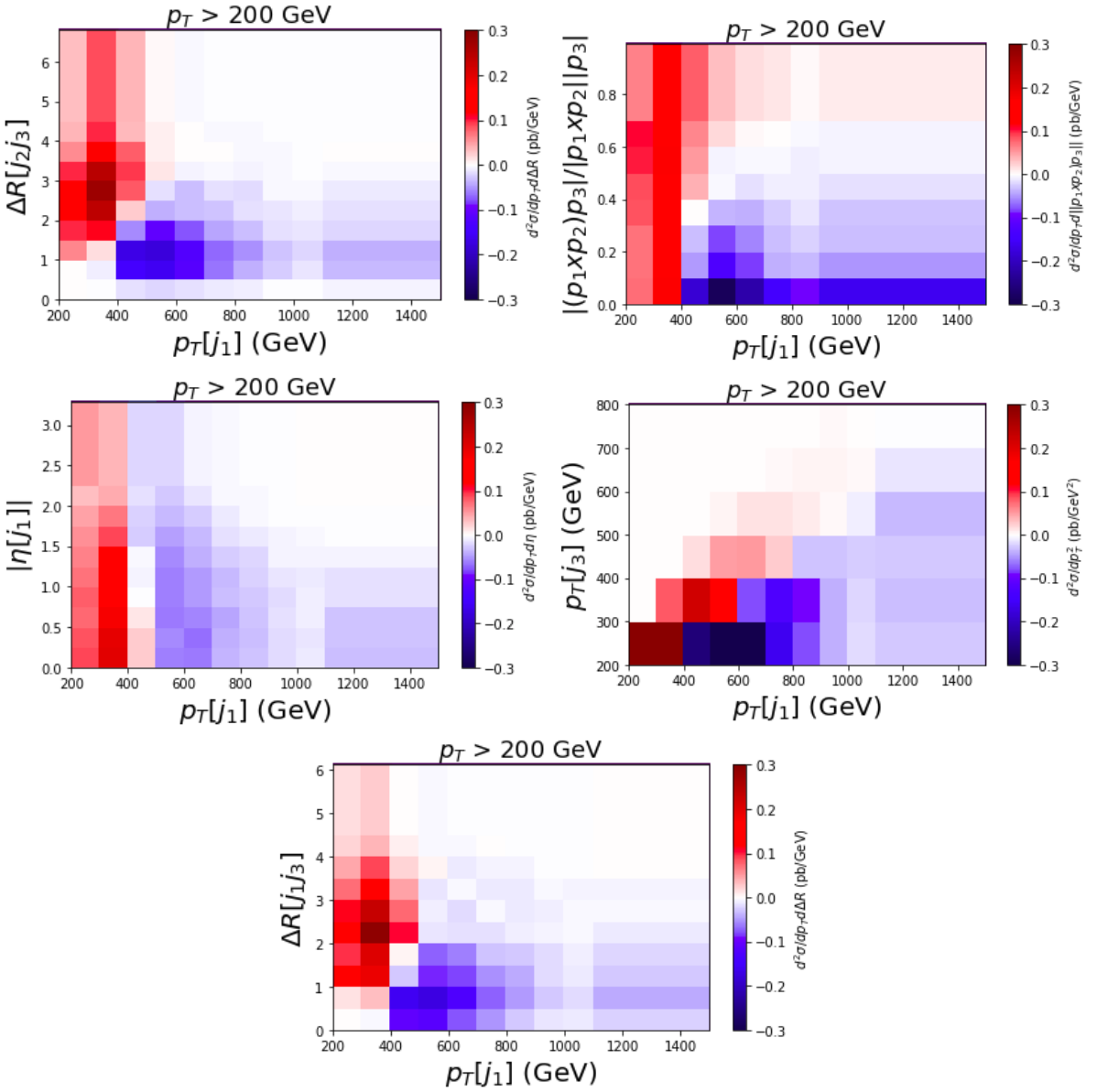

FIGURE 4.3.3. Examples of double differential distributions, for $p_T > 200$ GeV; all three involve the transverse momentum of the 1^{st} jet, respectively vs the angular distance between the 2^{nd} and 3^{rd} jets, the normalised triple product of the three jet momenta, the pseudorapidity of the 1^{st} jet, the transverse momentum of the 3^{rd} jet and the angular distance between the 1^{st} and the 3^{rd} jets. The relative binnings are described in Table 4.4; for the transverse momenta, the last bin is not entirely displayed. The total differential cross-section for each bin is codified in the color bar besides each plot, with red shades for the positive contributions and blue shades for the negative ones. The first 2 combinations are promising ones, since it is quite easy to isolate the differently colored regions of the plane, by considering some compact ranges for the variables; this is not true for the third plot, since the sign of the cross-section does not seem to depend in a significative way on the value of $|\eta[j_1]|$. The last two plots suggest the signs of the event weights are related to their topology

Distribution	Bin width	From	To	Number of bins
$p_T[j_1]$	20 GeV	200 GeV	1800 GeV + last bin	81
	40 GeV	200 GeV	1800 GeV + last bin	41
$p_T[j_2]$	40 GeV	200 GeV	1800 GeV + last bin	41
$\Delta R[j_2 j_3]$	0.1	0.4	6.6 + last bin	63
$\lvert\eta[j_1]\rvert$	0.1	0	3.2 + last bin	33
$\lvert\eta[j_3]\rvert$	0.1	0	3.8 + last bin	39
$\frac{\lvert(\boldsymbol{p_1}\times\boldsymbol{p_2})\cdot\boldsymbol{p_3}\rvert}{\lvert\boldsymbol{p_1}\times\boldsymbol{p_2}\rvert\lvert\boldsymbol{p_3}\rvert}$	0.02	0	1	50
Jet Broadening	0.02	0	1 + last bin	51
Transverse Thrust	0.02	0	1	50
$p_T[j_1]$ vs $p_T[j_3]$	100 GeV	200 GeV	1100 GeV + last bin	100
	100 GeV	200 GeV	1100 GeV + last bin	
$p_T[j_1]$ vs $\Delta R[j_2 j_3]$	100 GeV	200 GeV	1100 GeV + last bin	100
	0.5	0	4.5 + last bin	
$p_T[j_1]$ vs $\Delta R[j_1 j_3]$	100 GeV	200 GeV	1100 GeV + last bin	100
	0.5	0	4.5 + last bin	
$p_T[j_1]$ vs $\frac{\lvert(\boldsymbol{p_1}\times\boldsymbol{p_2})\cdot\boldsymbol{p_3}\rvert}{\lvert\boldsymbol{p_1}\times\boldsymbol{p_2}\rvert\lvert\boldsymbol{p_3}\rvert}$	100 GeV	200 GeV	900 GeV + last bin	64
	0.1	0	0.7 + last bin	
$p_T[j_1]$ vs $\lvert\eta[j_3]\rvert$	100 GeV	200 GeV	1400 GeV + last bin	169
	0.25	0	3 + last bin	
$p_T[j_1]$ vs Transverse Thrust	100 GeV	200 GeV	900 GeV + last bin	64
	0.1	0	0.7 + last bin	

TABLE 4.4. Binnings for the distributions used to set constraints on the C_G for $p_T > 200$ GeV. For double distributions, the first and the second rows refer to the first and the second variables, respectively. The total number of bins is shown on the last column, for each distribution. These binnings are chosen in order to guarantee the 10% accuracy over the SM analogous distributions: fine binnings are used for the single-variable distributions, while the double-differential ones present larger bins, so that enough events can be found in each of them. A larger last bin is present when the distribution tail does not contain enough events. For $p_T[j_1]$, two binnings are proposed, to show the effect of the binning on the C_G bounds

same sign than the weight, so a comparison has to be made to check the efficiency of our procedure.

To this extent, we calculate the matrix element for each event we generated in the interference sample and we count how many are there with a sign or the other. The matrix element depends on the momenta of the involved particles, the flavour and the helicities of the partons; among these quantities, though, only the final momenta of the jets are available in experiments. For this reason, we have to sum over all the possibilities for the variables we are blind at: this implies, for the set of momenta of each event, to sum above all the subprocesses that can take part to the three-jet production, varying the type of particles and summing all the helicity combinations of the incoming partons; moreover, all the permutations of the outgoing jets with the measured momenta have

Distribution	Upper bound on C_G	Lower bound on C_G
$p_T[j_1]$, bins of 20 GeV	$1.36{\cdot}10^{-1}$ ($4.06{\cdot}10^{-2}$)	$-1.36{\cdot}10^{-1}$ ($-3.19{\cdot}10^{-2}$)
$p_T[j_1]$, bins of 40 GeV	$1.53{\cdot}10^{-1}$ ($4.77{\cdot}10^{-2}$)	$-1.53{\cdot}10^{-1}$ ($-3.83{\cdot}10^{-2}$)
$p_T[j_1]$ vs $\lvert\eta[j_3]\rvert$	$1.59{\cdot}10^{-1}$ ($5.91{\cdot}10^{-2}$)	$-1.59{\cdot}10^{-1}$ ($-4.54{\cdot}10^{-2}$)
$p_T[j_1]$ vs $\Delta R[j_2 j_3]$	$2.90{\cdot}10^{-1}$ ($8.42{\cdot}10^{-2}$)	$-2.90{\cdot}10^{-1}$ ($-7.13{\cdot}10^{-2}$)
$\Delta R[j_2 j_3]$	$4.39{\cdot}10^{-1}$ ($2.20{\cdot}10^{-1}$)	$-4.39{\cdot}10^{-1}$ ($-2.43{\cdot}10^{-1}$)
$p_T[j_1]$ vs $\frac{\lvert(\boldsymbol{p_1}\times\boldsymbol{p_2})\cdot\boldsymbol{p_3}\rvert}{\lvert\boldsymbol{p_1}\times\boldsymbol{p_2}\rvert\lvert\boldsymbol{p_3}\rvert}$	$5.00{\cdot}10^{-1}$ ($9.98{\cdot}10^{-2}$)	$-5.00{\cdot}10^{-1}$ ($-9.27{\cdot}10^{-2}$)
$p_T[j_1]$ vs Transverse Thrust	$5.83{\cdot}10^{-1}$ ($1.04{\cdot}10^{-1}$)	$-5.83{\cdot}10^{-1}$ ($-9.36{\cdot}10^{-2}$)
$\frac{\lvert(\boldsymbol{p_1}\times\boldsymbol{p_2})\cdot\boldsymbol{p_3}\rvert}{\lvert\boldsymbol{p_1}\times\boldsymbol{p_2}\rvert\lvert\boldsymbol{p_3}\rvert}$	$6.29{\cdot}10^{-1}$ ($2.11{\cdot}10^{-1}$)	$-6.29{\cdot}10^{-1}$ ($-2.45{\cdot}10^{-1}$)
Jet Broadening	$8.41{\cdot}10^{-1}$ ($1.46{\cdot}10^{-1}$)	$-8.41{\cdot}10^{-1}$ ($-1.37{\cdot}10^{-1}$)
Transverse Thrust	$9.76{\cdot}10^{-1}$ ($2.30{\cdot}10^{-1}$)	$-9.76{\cdot}10^{-1}$ ($-2.51{\cdot}10^{-1}$)
$\lvert\eta[j_3]\rvert$	1.11 ($2.62{\cdot}10^{-1}$)	-1.11 ($-2.44{\cdot}10^{-1}$)
$\lvert\eta[j_1]\rvert$	3.33 ($2.55{\cdot}10^{-1}$)	-3.33 ($2.60{\cdot}10^{-1}$)

TABLE 4.5. Bounds on the coefficient using different variables, inferred using all the data in the distributions for p_T >200 GeV, for Λ =1 TeV. In each column, the first numbers are obtained through the $\mathcal{O}(\Lambda^{-2})$ contribution only, the ones into brackets take into account the $\mathcal{O}(\Lambda^{-4})$ data, too. For $p_T[j_1]$, the results from two binnings are shown

to taken into account in the summation. Furthermore, the incoming partons have to be weighted by the PDF, to take into account their relative luminosity: the one we consider is the same used in the calculations, the NNPDF2.3. Up to this point, having set a fixed renormalisation scale, at 500 GeV, for all the events in the $p_T > 200$ GeV sample, avoids the introduction of an event-by-event renormalisation, simplifying the calculations.
As a consequence of this matrix element weighting, this procedure is not able to divide perfectly the positive- from the negative-weighted events, as it would have done if we knew all the information about each sample, but still provides the best discrimination that we can reach through the available experimental data. Over a sample of 100000 events, the region where the weighted matrix element is positive contains an excess of 36287 positive weights, while the region where the weighted matrix element is negative shows an excess of 33901 negative ones. As it is shown in Table 4.3, the p_T >200 GeV sample contains 51200 positive- and 48800 negative-weighted events, so the loss is only of 29.1% for the positive weights and of 30.5% of the negative ones, even after the sum over the subprocesses and the helicities. This result is the one to which the event splittings we obtain by cutting on the variables we chose have to be compared, in order to estimate how good they are in the identification of the phase space regions with different cross-section signs.
The results are shown in Table 4.6; the best single-variable distribution in differentiating the events is the transverse thrust; as it can be seen from the plot in Fig. 4.3.1, a cut at 0.1 isolates the different regions in which more positive- than negative-weighted events are present, and viceversa: by applying these cuts on the events, we are able to catch 50% of the positive weights and 46.5% of the negative ones. The transverse momentum of the 1^{st} jet achieve similar results. The best divisions come from the double differential distributions; for the $p_T[j_1]$ vs $\Delta R[j_1 j_2]$ one, the plot in Fig. 4.3.3 suggests a cut, on

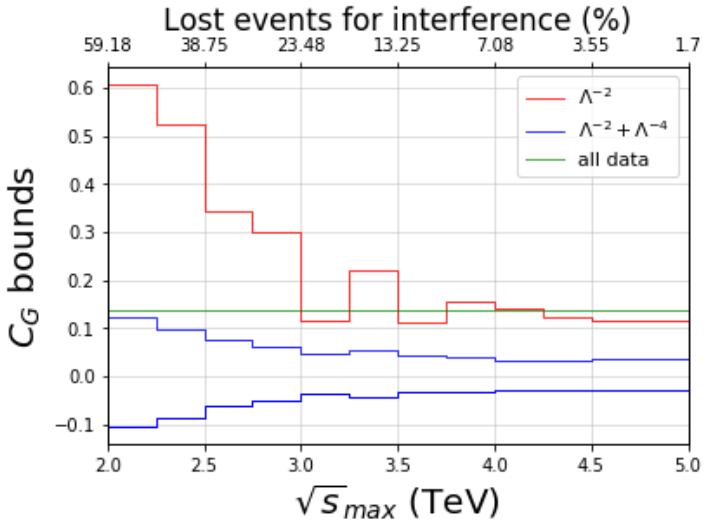

FIGURE 4.3.4. Bounds on C_G as functions of an upper cut over the center-of-mass energy, $\sqrt{s}$, inferred from the $p_T[j_1]$ distribution with bins of 40 GeV, for $\Lambda = 1$ TeV. The red line shows the bounds from the $\mathcal{O}(\Lambda^{-2})$ order only, while the blue ones take into account the $\mathcal{O}(\Lambda^{-4})$ contribution, too. Only the upper bounds from the interference are shown, since the lower ones are symmetric to them with respect to the horizontal axis. The gren line reports the bounds from the interference, obtained using all the events. The axis on top of the plot reports the percentage of events, in the interference sample, that get lost when imposing the corresponding cut on the energy

the two-variable plane, along a diagonal line through the origin and between the red and blue regions: in this way, the 48.1% of the positive and the 44.4% of the negative weights are correctly divided.
The results from these variables are in any case better than the division by the interference cross-section which, as it is stated in Table 4.3, shows a difference of 2400 between the positive- and negative-weighted events, over a sample of 100000 ones.

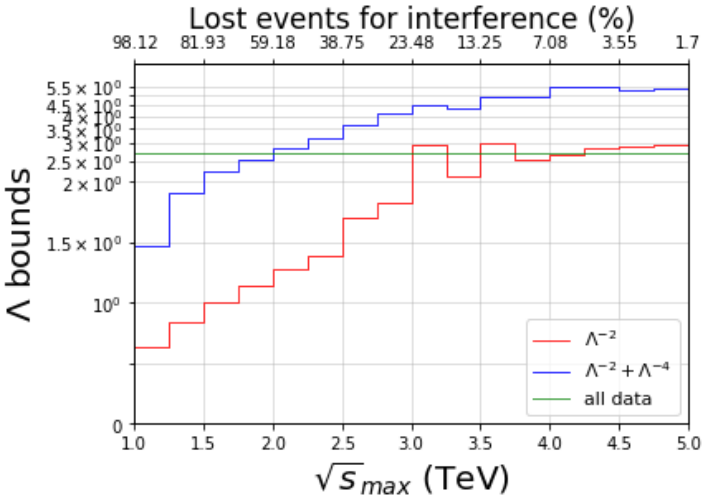

FIGURE 4.3.5. Upper bounds on Λ as functions of an upper cut over the center-of-mass energy, $\sqrt{s}$, inferred from the $p_T[j_1]$ distribution with bins of 40 GeV, for $C_G = 1$. The red line shows the bounds from the $\mathcal{O}(\Lambda^{-2})$ order only, while the blue one takes into account the $\mathcal{O}(\Lambda^{-4})$ contribution, too. The gren line reports the bounds from the interference, obtained using all the events. The axis on top of the plot reports the percentage of events, in the interference sample, that get lost when imposing the corresponding cut on the energy

Distribution	Range	wgt>0 - wgt<0	comparison to matrix element
$p_T[j_1]$ vs $\Delta R[j_2 j_3]$	$\Delta R > 3.75 \cdot 10^{-3} \cdot (p_T/GeV)$	17445	48.1%
	$\Delta R < 3.75 \cdot 10^{-3} \cdot (p_T/GeV)$	-15059	44.4%
Transverse Thrust	>0.1	18141	50.0%
	<0.1	-15755	46.5%
$p_T[j_1]$	<440 GeV	16314	45.0%
	>440 GeV	-13928	41.1%
$\Delta R[j_2 j_3]$	>1.8	14068	38.8%
	<1.8	-11682	34.5%
$\frac{\lvert(\boldsymbol{p_1}\times\boldsymbol{p_2})\cdot\boldsymbol{p_3}\rvert}{\lvert\boldsymbol{p_1}\times\boldsymbol{p_2}\rvert\lvert\boldsymbol{p_3}\rvert}$	>0.28	5483	15.1%
	<0.28	-3097	9.1%
$\lvert\eta[j_3]\rvert$	>1.2	3399	9.4%
	<1.2	-1013	3.0%
Total cross-section	-	2400	2.4%

TABLE 4.6. Comparison between the estimation of positive- and negative-weighted events, through cuts on the variables and the weighted matrix elements, for p_T >200 GeV. The values of the cuts are shown: they are inferred from the plots in Fig. 4.3.1 and Fig. 4.3.3. The numbers in the last two columns are the differences between the number of positive- and negative-weighted events in the variable ranges, for 100000 events, and their percentage with respect to the weighted matrix element results (36287 positive weights and 33901 negative ones). The difference provided by the total interference cross-section is reported too

5. Conclusions

In this work, we analised the cancellation of the contribution to the cross-section, for the interference among the SM and the O_G operator, introduced in the SMEFT framework and providing modifications to the gluon vertices. The analysis is based on the idea that the interference is not necessarily positive and, even if its total cross-section is almost null, this is not necessarily true for the differential distribution, as a cancellation can occur between different phase space regions whose contributions have different signs. By generating event samples for three-jet production through the Monte Carlo simulator Madgraph5@NLO, we checked different variables which are usually taken into account in jet analysis, obtaining that some of them are sensitive to the sign of the events, and therefore it is possible to separate zones with more positive- than negative-weighted events by imposing cuts on their values. These quantities are the transverse momentum of the 1^{st} jet, the angular distance between the 2^{nd} and the 3^{rd} jets, the pseudorapidity of the 3^{rd} jet, the normalised triple product of the three-momenta of the jets, the total jet broadening and the transverse thrust, and the double-differential distributions involving pairs of these. Some of these observables are strictly realted to the event topology, some other are not.
Using the distribution of these variables over the interference events, we assumed the SM distributions as the experimental data and we set constraints on the value of the C_G coefficient of the O_G operator; the best one comes from the transverse momentum of the 1^{st} jet and reads $C_G < 1.36 \cdot 10^{-1}$ at 68% CL, for a new physics scale $\Lambda = 1$ TeV.
We checked the maximum division between positive and negative weights that can be experimentally achieved, through the matrix element weighting, obtaining that suitable cuts on the transverse thrust, the transverse momentum or the angular distance mentioned above can do the same job with an efficiency of almost 50%, but with easier measurements and procedures.

Bibliography

[1] S.F. Novaes, *Standard Model: An Introduction*, [0001283v1] (2000)

[2] A. Salam, J.C. Ward, *On a gauge theory of elementary interactions, Nuovo Cim.* **19**, 165 (1961)

[3] S.L. Glashow, *Partial Symmetries of Weak Interactions, Nucl. Phys* **22**, 579-588 (1961)

[4] S. Weinberg, *A Model of Leptons, Phys. Rev. Lett.* **19**, 1264 (1967)

[5] S.L. Glashow, J. Iliopoulos, L. Maiani, *Weak Interactions with Lepton-Hadron Symmetry, Phys. Rev. D* **2**, 1285 (1970)

[6] G. Polesello, *Introduction to LHC physics*, Journal of Physics: Conference Series **53**, 107-116 (2006)

[7] R.N. Mohapatra, G. Senjanovic, *Exact Left-Right Symmetry and Spontaneous Violation of Parity, Phys. Rev. D* **12**, 1512-1523 (1975)

[8] A. Halprin, P. Minkowski, H. Primakoff, S.P. Rosen, *Double-beta decay and a massive Majorana neutrino, Phys. Rev. D* **13**, 2567-2571 (1976)

[9] A.D. Sakharov, *Violation of CP invariance, C asymmetry, and baryon asymmetry of the universe*, Pisma Zh. Eksp. Teor. Fiz. 5 32 (1967)

[10] A.J. Buras, J.R. Ellis, M.K. Gaillard, D.V. Nanopoulos, *Aspects of the grand unification of strong, weak and electromagnetic interactions, Nucl. Phys. B* **135**, 66 (1978)

[11] S.P. Martin, *A supersymmetry primer*, Adv. Ser. Direct. High Energy Phys. 21 1 (2010)

[12] G. 't Hooft, *Symmetry Breaking through Bell-Jackiw Anomalies, Phys. Rev. Lett.* **37**, 8 (1976)

[13] T. Appelquist, J. Carazzone, *Infrared Singularities and Massive Fields, Phys. Rev. D* **11**, 2856 (1975)

[14] A.V. Manohar, *Introduction to Effective Field Theories*, [1804.05863v1] (2018)

[15] I. Brivio, M. Trott, *The Standard Model as an Effective Field Theory*, [1706.08945v3] (2018)

[16] C. Smith, *Minimal Flavor Violation*, High Energy Physics - Phenomenology [hep-ph], Université Grenoble Alpes (2015)

[17] L. Lehman, A. Martin, *Low-derivative operators of the Standard Model effective field theory via Hilbert series methods, JHEP* **02**, 081, [1510.00372] (2016)

[18] A. Kobach, *Baryon Number, Lepton Number, and Operator Dimension in the Standard Model, Phys. Lett.* **B758**, 455–457 (2016)

[19] B. Grzadkowski, M. Iskrzyński, M. Misiak, J. Rosiek, *Dimension-Six Terms in the Standard Model Lagrangian*, 1008.4884v3 (2017)

[20] W. Buchmüller, D. Wiler, *Effective lagrangian analysis of new interactions and flavour conservation, Nucl. Phys. B* **286**, 621 (1986)

[21] A. Falkowski, M. González, K. Mimouni, *Compilation of low-energy constraints on 4-fermion operators in the SMEFT*, [1706.03783] (2017)

[22] W. Dekens, J. de Vries, *Renormalization Group Running of Dimension-Six Sources of Parity and Time-Reversal Violation, JHEP* **05** 149, [1303.3156] (2013)

[23] E.H. Simmons, *Higher dimension gluon operators and hadronic scattering, Phys. Lett. B* **246**, 471-476 (1990)

[24] C. Zhang, S. Willenbrock, *Effective-Field-Theory Approach to Top-Quark Production and Decay*, [1008.3869v3]

[25] V. Hirschi, F. Maltoni, I. Tsinikos, E. Vryonidou, *Constraining anomalous gluon self-interactions at LHC: a reappraisal*, [1806.04696v2] (2018)

[26] F. Krauss, S. Kuttimalai, T. Plenh, *LHC multijet events as a probe for anomalous dimension-six gluon interactions*, [1611.00767v3] (2017)

[27] R. Goldouzian, M.D. Hildreth, *LHC dijet angular distributions as a probe for the dimension-six triple gluon vertex*, [2001.02736v1] (2020)
[28] CMS Collaboration, *Study of hadronic event-shape variables in multijet final states in pp collisions at* $\sqrt{s}$ *= 7 TeV, JHEP* **10** 087, [1407.2856v2] (2014)
[29] C. Degrande, *Implementation of the top effective-field theory for MG5*, https://cp3.irmp.ucl.ac.be/projects/madgraph/attachment/wiki/Models/TopEffTh/note.pdf (2015)
[30] C. Degrande, C. Duhr, B. Fuks, D. Grellscheid, O. Mattelaer et al., *UFO - The Universal FeynRules output, Comput.Phys.Commun.* **183**, [1108.2040] (2012)
[31] A. Alloul, N.D. Christensen, C. Degrande, C. Duhr, B. Fuks, *FeynRules 2.0 - A complete toolbox for tree-level phenomenology, Comput.Phys.Commun.* **185**, [1310.1921] (2014)
[32] J. Alwall, R. Frederix, S. Frixione, V. Hirschi, F. Maltoni et al., *The automated computation of tree-level and next-to-leading order differential cross-sections, and their matching to parton shower simulations, JHEP* **1407** 079, [1405.0301] (2014)
[33] O. Mattelaer, *A new approach to matrix element re-weighting*, http://hdl.handle.net/2078.1/69114 (2011)
[34] ATLAS Collaboration, *Measurements of the three-jet production cross-sections in pp collisions at 7 TeV centre-of-mass energy using the ATLAS detector*, [1411.1855v2] (2015)
[35] ATLAS Collaboration, *Luminosity determination in pp collisions at* $\sqrt{s}$ *=13 TeV using the ATLAS detector at the LHC*, ATLAS-CONF-2019-021 (2019)